

2

AD-A264 020



RL-TR-92-320
Final Technical Report
December 1992

S DTIC
ELECTE
MAY 1 1 1993
C **D**



QUANTIFICATION OF THERMOGRAPHIC MAPPING TECHNIQUES

University of Colorado

Dr. John Norgard, Don Metzger

APPROVED FOR PUBLIC RELEASE; DISTRIBUTION UNLIMITED.

93 5 07 02 5

93-10074



Rome Laboratory
Air Force Materiel Command
Griffiss Air Force Base, New York

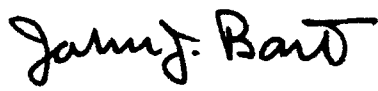
This report has been reviewed by the Rome Laboratory Public Affairs Office (PA) and is releasable to the National Technical Information Service (NTIS). At NTIS it will be releasable to the general public, including foreign nations.

RL-TR-92-320 has been reviewed and is approved for publication.

APPROVED:


MICHAEL F. SEIFERT
Project Engineer

FOR THE COMMANDER


JOHN J. BART, Chief Scientist
Reliability Sciences

If your address has changed or if you wish to be removed from the Rome Laboratory mailing list, or if the addressee is no longer employed by your organization, please notify RL (ERPT) Griffiss AFB NY 13441. This will assist us in maintaining a current mailing list.

Do not return copies of this report unless contractual obligations or notices on a specific document require that it be returned.

REPORT DOCUMENTATION PAGE

Form Approved
OMB No. 0704-0188

Public reporting burden for this collection of information is estimated to average 1 hour per response, including the time for reviewing instructions, searching existing data sources, gathering and maintaining the data needed, and completing and reviewing the collection of information. Send comments regarding this burden estimate or any other aspect of this collection of information, including suggestions for reducing this burden, to Washington Headquarters Services, Directorate for Information Operations and Reports, 1215 Jefferson Davis Highway, Suite 1204, Arlington, VA 22202-4302, and to the Office of Management and Budget, Paperwork Reduction Project (0704-0188), Washington, DC 20503.

1. AGENCY USE ONLY (Leave Blank)		2. REPORT DATE December 1992		3. REPORT TYPE AND DATES COVERED Final Aug 92 - Jan 92	
4. TITLE AND SUBTITLE QUANTIFICATION OF THERMOGRAPHIC MAPPING TECHNIQUES				5. FUNDING NUMBERS C - F30602-91-C-0113 PE - 64735F PR - 3321 TA - 03 WU - P1	
6. AUTHOR(S) Dr John Norgard, Don Metzger				7. PERFORMING ORGANIZATION REPORT NUMBER N/A	
7. PERFORMING ORGANIZATION NAME(S) AND ADDRESS(ES) University of Colorado Colorado Springs CO 80933-7150				8. PERFORMING ORGANIZATION REPORT NUMBER N/A	
9. SPONSORING/MONITORING AGENCY NAME(S) AND ADDRESS(ES) Rome Laboratory (ERPT) 525 Brooks Road Griffiss AFB NY 13441-4505				10. SPONSORING/MONITORING AGENCY REPORT NUMBER RL-TR-92-320	
11. SUPPLEMENTARY NOTES Georgia Institute of Technology Subcontract to University of Colorado. Rome Laboratory Project Engineer: Michael F. Seifert/ERPT/(315) 330-7642					
12a. DISTRIBUTION/AVAILABILITY STATEMENT Approved for public release; distribution unlimited.				12b. DISTRIBUTION CODE	
13. ABSTRACT (Maximum 200 words) Thermographic mapping of microwave fields is a method of imaging the electromagnetic field in a region of space by viewing the heating it produces when interacting with a material. As the microwave field interacts with a material, some of the electromagnetic energy may be converted into heat. This heat can be viewed in several ways; the most useful technique developed to date involves an infrared camera. The objective of this work is to develop appropriate theoretical and experimental practices to allow for the design and manufacture of an electromagnetic absorbing screen. The absorbing screen must exhibit a significant heat rise for a small amount of incident electromagnetic energy while not disturbing the electromagnetic field it is measuring. Thus, the design of the absorber involves a trade-off between these two desirable properties.					
14. SUBJECT TERMS Thermographic Mapping, Infrared (IR) Camera, Electromagnetic Energy				15. NUMBER OF PAGES 92	
				16. PRICE CODE	
17. SECURITY CLASSIFICATION OF REPORT UNCLASSIFIED		18. SECURITY CLASSIFICATION OF THIS PAGE UNCLASSIFIED		19. SECURITY CLASSIFICATION OF ABSTRACT UNCLASSIFIED	
				20. LIMITATION OF ABSTRACT UL	

Table of Contents

1	Introduction.....	1
2	Electromagnetic Theory.....	2
2.1	General Description of the Problem.....	2
2.2	Electromagnetic Analysis.....	2
2.2.1	Conservation of Power in a General Medium.....	3
2.2.2	Physical Interpretation of Complex Material Parameters.....	7
2.2.2.1	Polarization Loss.....	7
2.2.2.2	Magnetization Loss.....	9
2.2.2.3	Conduction Loss.....	9
2.2.3	Power Absorbed Related to Field Orientation.....	10
3	Design of an Absorbing Screen.....	12
3.1	Plane Waves Incident on an Absorbing Screen.....	12
3.1.1	Parallel Polarization.....	13
3.1.2	Perpendicular Polarization.....	16
3.1.3	Normal Incidence.....	18
3.2	Power Absorbed in the Screen.....	18
3.3	Power Reflected by the Screen.....	28
3.4	The Ratio of Absorbed and Reflected Power.....	31
3.5	Absorber Materials.....	34
3.6	Recipe for Preparation of Absorber.....	34
4	Measurement of the Electromagnetic Properties of the Absorber.....	36
4.1	Analysis of a Section of Lossy Dielectric in a Coaxial Airline.....	36
4.2	Relating Material Parameters to Measured S-Parameters.....	39
4.3	Data Processing for the Determination of Material Parameters.....	40
4.3.1	Resolving Multiple Solutions by Velocity Considerations.....	40
4.3.2	Network Analyzer Reference Plane Adjustment.....	41
4.4	Measurement Equipment and Procedures.....	42
4.5	Material Measurement Results.....	43
4.5.1	Comparison with Other Measurements.....	45
4.5.2	Results for Loaded Epoxies.....	45
4.6	DC Conductivity Measurements.....	60
	References.....	62
	Appendix A Mathematica Equations for Electromagnetic Analyses.....	62
A.1	Absorber Equations.....	62
A.2	Absorber Design Equations.....	65
A.3	Absorber Design Equations for Complex Material Parameters.....	67
	Appendix B Computer Processing of Material Parameter Data.....	69

List of Figures

Fig. 2-1 Overview of the problem for analysis.....	3
Fig. 2-2 A plane wave normally incident on a boundary between 2 materials	7
Fig. 2-3 Polarization of a dielectric sheet.....	8
Fig. 2-4 Electromagnetic fields in three regions.....	11
Fig. 3-1 A general plane wave in a planar 3-region geometry.....	13
Fig. 3-2 A parallel polarized plane wave in a planar 3-region geometry.....	14
Fig. 3-3 A perpendicularly polarized plane wave in a planar 3-region geometry	16
Fig. 3-4 %Pabs vs thickness and conductivity.....	22
Fig. 3-5 %Pabs vs frequency and thickness	23
Fig. 3-6 %Pabs vs relative permittivity and thickness	24
Fig. 3-7 %Pabs vs relative permittivity and frequency.....	25
Fig. 3-8 %Pabs vs conductivity and frequency	26
Fig. 3-9 %Pabs vs thickness	27
Fig. 3-10 %Pabs vs thickness for a thin absorber.....	27
Fig. 3-11 %Prefl vs thickness and conductivity	29
Fig. 3-12 %Prefl vs relative permittivity and frequency.....	30
Fig. 3-13 %Prefl vs thickness.....	31
Fig. 3-14 %Prefl vs thickness for a thin absorber.....	31
Fig. 3-15 %Pabs/%Prefl vs thickness and conductivity.....	32
Fig. 3-16 %Pabs/%Prefl vs thickness.....	33
Fig. 3-17 %Pabs/%Prefl vs thickness for a thin absorber	33
Fig. 4-1 Lossy dielectric section in a coaxial airline.....	37
Fig. 4-2 Network analyzer reference plane movement.....	42
Fig. 4-3 Real permittivity and permeability of air.....	44
Fig. 4-4 Imaginary permittivity and permeability of air.....	44
Fig. 4-5 Real permittivity and permeability of teflon.....	46
Fig. 4-6 Imaginary permittivity and permeability of teflon.....	46
Fig. 4-7 Real permittivity and permeability of nylon.....	47
Fig. 4-8 Imaginary permittivity and permeability of nylon.....	47
Fig. 4-9 Real permittivity and permeability of 20% ferrite loaded epoxy.....	48
Fig. 4-10 Imaginary permittivity, permeability and effective conductivity of 20% ferrite loaded epoxy.....	49
Fig. 4-11 Real permittivity and permeability of 30% ferrite loaded epoxy	50
Fig. 4-12 Imaginary permittivity, permeability and effective conductivity of 30% ferrite loaded epoxy.....	51
Fig. 4-13 Real permittivity and permeability of 40% ferrite loaded epoxy	52
Fig. 4-14 Imaginary permittivity, permeability and effective conductivity of 40% ferrite loaded epoxy.....	53
Fig. 4-15 Real permittivity and permeability of 1.7% carbon loaded epoxy	54

Fig. 4-16 Imaginary permittivity, permeability and effective conductivity of 1.7% carbon loaded epoxy.....55

Fig. 4-17 Real permittivity and permeability of 4% carbon loaded epoxy.....56

Fig. 4-18 Imaginary permittivity, permeability and effective conductivity of 4% carbon loaded epoxy.....57

Fig. 4-19 Real permittivity and permeability of 2.3% carbon-22.5% ferrite loaded epoxy58

Fig. 4-20 Imaginary permittivity, permeability and effective conductivity of 2.3% carbon-22.5% ferrite loaded epoxy59

Fig. 4-21 DC Measurement of Conductivity.....61

Fig. 4-22 Extrapolated effective conductivity for 4% carbon loaded epoxy.....61

DTIC QUALITY INSPECTION 5

Accession For	
NTIS CRA&I	<input checked="" type="checkbox"/>
DTIC TAB	<input type="checkbox"/>
Unannounced	<input type="checkbox"/>
Justification	
By	
Distribution /	
Availability Codes	
Dist	Avail and/or Special
A-1	

List of Tables

Table 4-1	20% ferrite recipe	49
Table 4-2	30% ferrite recipe	49
Table 4-3	40% ferrite recipe	50
Table 4-4	1.7% carbon recipe	55
Table 4-5	4% carbon recipe	55
Table 4-6	2.3% carbon-22.5% ferrite recipe	59
Table 4-7	Material parameters for prepared samples	60

1 Introduction

Thermographic mapping of microwave fields is a method of imaging the electromagnetic field in a region of space by viewing the heating it produces when interacting with a material. Many people are familiar with the effects of microwaves on materials through the wide-spread use of microwave ovens. As the microwave field interacts with a lossy material, some of the electromagnetic energy may be converted into heat. This heat can be viewed in several ways [1], the most useful technique developed to date involves an infrared camera.

This method of measuring microwave fields has two major advantages over conventional methods involving metallic probes. First, the field-of-view of the camera is usually digitized into at least 128 by 128 independent measurements of the microwave field, yielding more information in a shorter time. Second, the material which heats in the microwave field is less perturbing to that field than the introduction of a metallic probe, yielding more accurate measurements. The primary limitation up to this time has been an inability to associate a microwave field strength with an observed temperature.

The objective of this work is to develop appropriate theoretical and experimental practices to allow for the design and manufacture of an electromagnetic absorbing screen which will allow an infrared image to be converted into a microwave field strength.

An exhaustive development of the pertinent electromagnetic theory is given first. This is then applied to the problem of optimizing the dielectric constant, conductivity and thickness of a planar absorber in order to maximize the power absorption under plane wave illumination. A particular variety of absorber, a carbon or ferrite loaded epoxy, is then manufactured. A method is developed to measure the complex permittivity and permeability of the constructed absorber at microwave frequencies. The end result of this work is an absorber with known electrical characteristics.

This work addresses the electrical characteristics of an absorbing material. In addition, it is necessary to characterize the thermal properties of the absorber and to understand how the heat deposited by the microwaves redistributes within the absorber. With proper understanding of these three issues, it will be possible to associate a microwave field strength with an observed temperature from the infrared camera.

2 Electromagnetic Theory

This section describes the mechanisms through which electromagnetic energy is deposited in a material in the form of heat. The heat deposition is controlled by the electromagnetic field strength, spatial distribution, orientation and the electromagnetic properties of the material. The heat flow and final temperature profile are controlled by the thermal properties of the material and the ambient temperature. The emphasis of this discussion will be on the electromagnetic considerations.

2.1 General Description of the Problem

The geometry under consideration is shown in Fig. 2-1. A slab of microwave absorber is entirely surrounded by styrofoam. (The section of foam on the right side of the absorber has been removed so that the conduction effects can be illustrated.) The foam provides a thermal insulation, but has very little interaction with the microwave field. For the purposes of this study, the effects of the styrofoam on the microwave field will be ignored. The microwaves interact with the absorber and deposit energy in the form of heat. This heat can redistribute throughout the absorber by means of the thermal conductivity. In addition, the heat can leave the absorber through conduction, convection and radiation from any of its sides. Because the styrofoam next to the sides of the absorber will heat to the same temperature as the absorber, radiation from all sides except the top can be considered as negligible. Because the styrofoam touches every side except the top, convection from all sides except the top, can be ignored. The total amount of heat lost due to convection is proportional to surface area. The thickness of the slab will typically be small so as to resemble a thin sheet. Therefore, the heat lost through the thin edges can be ignored, leaving only the heat conducted through the bottom of the sheet into the styrofoam base. Finally, the sheet of absorber is placed horizontally so that the convection will not distort the heating. Analysis of the thermal parts of this problem will be left for future research.

2.2 Electromagnetic Analysis

First, the electromagnetic aspects of the problem outlined above will be discussed. This will include considerations of how heat is formed in a

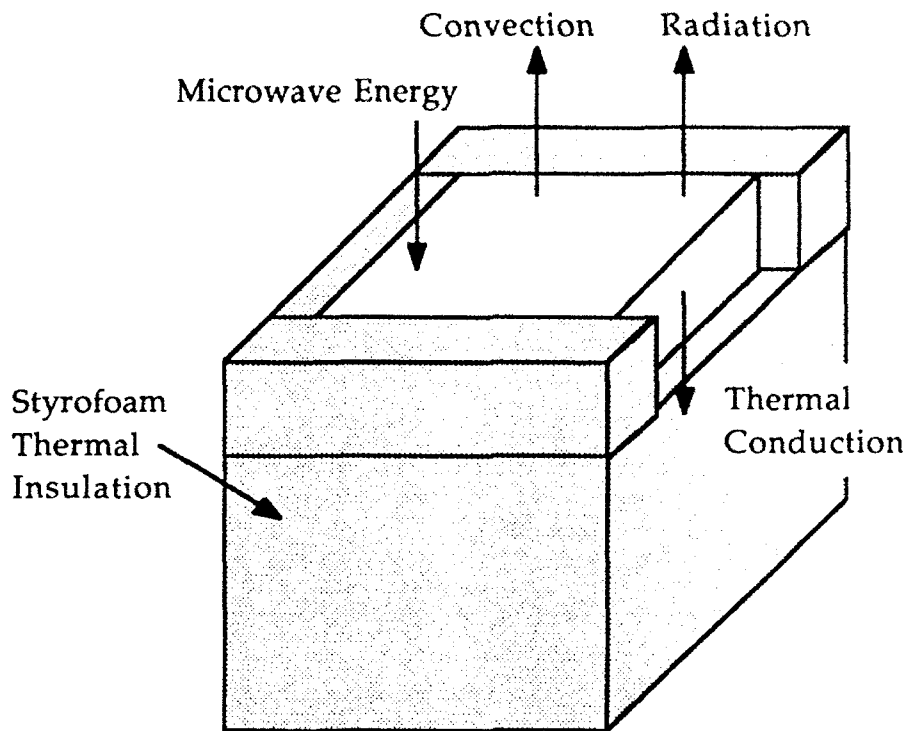


Fig. 2-1 Overview of the problem for analysis.

material in the presence of an electromagnetic field. A brief discussion will be given to provide physical understanding for the electromagnetic parameters of a material. Attention will be given to how the orientation of the field to a thin absorbing screen affects the heating. The objective of this section is to adequately describe the significant factors which determine how much electromagnetic energy is deposited in a material.

2.2.1 Conservation of Power in a General Medium

The constitutive equations relating field quantities and material parameters in the frequency domain are

$$\begin{aligned}\bar{\mathbf{D}} &= \epsilon \bar{\mathbf{E}} \\ \bar{\mathbf{B}} &= \mu \bar{\mathbf{H}} \\ \bar{\mathbf{J}} &= \sigma \bar{\mathbf{E}} + \bar{\mathbf{J}}_a\end{aligned}$$

In the last equation, \mathbf{J}_a represents an applied or source volumetric current. The material parameters are allowed to be complex:

$$\begin{aligned}\epsilon &= \epsilon' - j\epsilon'' \\ \mu &= \mu' - j\mu'' \\ \sigma &= \sigma' - j\sigma''\end{aligned}$$

This allows, for example, \mathbf{D} to have both magnitude difference and phase lag with respect to \mathbf{E} at a given frequency. For this work, the material parameters are considered to be frequency domain quantities which may be functions of

frequency. Although it is unlikely that any real materials require all three quantities to be complex, this theory will cover the most general case. Also, in order to allow for generality, a magnetic current term will be included only as a source, thus the volumetric magnetic current density is

$$\vec{M} = \vec{M}_a$$

Ampere's law is

$$\nabla \times \vec{H} = j\omega\vec{D} + \vec{J}$$

Substituting for D and J from above yields

$$\nabla \times \vec{H} = j\omega\epsilon\vec{E} + \sigma\vec{E} + \vec{J}_a$$

Putting in the complex expressions for the material parameters gives

$$\nabla \times \vec{H} = j\omega(\epsilon' - j\epsilon'')\vec{E} + (\sigma' - j\sigma'')\vec{E} + \vec{J}_a$$

Forming the complex conjugate of both sides and separating the real and imaginary parts of the E multiplier gives the result

$$\begin{aligned}\nabla \times \vec{H}^* &= -j\omega(\epsilon' + j\epsilon'')\vec{E}^* + (\sigma' + j\sigma'')\vec{E}^* + \vec{J}_a^* \\ \nabla \times \vec{H}^* &= [(\sigma' + \omega\epsilon'') + j(\sigma'' - \omega\epsilon')] \vec{E}^* + \vec{J}_a^*\end{aligned}\quad (2-1)$$

We will return to this result shortly.

Faraday's law is

$$\nabla \times \vec{E} = -j\omega\vec{B} - \vec{M}$$

Substituting for B and M from above yields

$$\nabla \times \vec{E} = -j\omega\mu\vec{H} - \vec{M}_a$$

Putting in the complex expressions for the material parameters gives

$$\nabla \times \vec{E} = -j\omega(\mu' - j\mu'')\vec{H} - \vec{M}_a$$

Now, form the vector inner product of both sides with the complex conjugate of the magnetic field H.

$$(\nabla \times \vec{E}) \cdot \vec{H}^* = -(\omega\mu'' + j\omega\mu')\vec{H} \cdot \vec{H}^* - \vec{M}_a \cdot \vec{H}^*$$

The left side can be simplified by means of the vector identity

$$(\nabla \times \vec{A}) \cdot \vec{B} = \nabla \cdot (\vec{A} \times \vec{B}) + \vec{A} \cdot (\nabla \times \vec{B})$$

which yields

$$\nabla \cdot (\vec{E} \times \vec{H}^*) + \vec{E} \cdot (\nabla \times \vec{H}^*) = -(\omega\mu'' + j\omega\mu')\vec{H} \cdot \vec{H}^* - \vec{M}_a \cdot \vec{H}^*$$

Substituting equation 2-1 into this yields

$$\nabla \cdot (\vec{E} \times \vec{H}^*) + \vec{E} \cdot [(\sigma' + \omega\epsilon'') + j(\sigma'' - \omega\epsilon')] \vec{E}^* + \vec{E} \cdot \vec{J}_a^* = -(\omega\mu'' + j\omega\mu')\vec{H} \cdot \vec{H}^* - \vec{M}_a \cdot \vec{H}^*$$

The identity for the modulus of complex numbers

$$\vec{A} \cdot \vec{A}^* = |\vec{A}|^2 = A^2$$

can be used to simplify some of the dot products. Using this identity and rearranging gives

$$\nabla \cdot (\bar{\mathbf{E}} \times \bar{\mathbf{H}}^*) = -[(\sigma' + \omega\epsilon'') + j(\sigma'' - \omega\epsilon')]E^2 - \bar{\mathbf{E}} \cdot \bar{\mathbf{J}}_a^* - (\omega\mu'' + j\omega\mu')H^2 - \bar{\mathbf{M}}_a \cdot \bar{\mathbf{H}}^*$$

Now, taking the volume integral of both sides yields

$$\iiint_V \nabla \cdot (\bar{\mathbf{E}} \times \bar{\mathbf{H}}^*) dv = -\iiint_V (\sigma' + \omega\epsilon'')E^2 + \omega\mu''H^2 dv - \iiint_V \bar{\mathbf{M}}_a \cdot \bar{\mathbf{H}}^* + \bar{\mathbf{E}} \cdot \bar{\mathbf{J}}_a^* dv - \\ j\iiint_V (\sigma'' - \omega\epsilon')E^2 + \omega\mu'H^2 dv$$

The left hand side can be reduced by the divergence theorem. Rearranging yields

$$-\frac{1}{2}\iiint_V \bar{\mathbf{M}}_a \cdot \bar{\mathbf{H}}^* + \bar{\mathbf{E}} \cdot \bar{\mathbf{J}}_a^* dv = \frac{1}{2}\oint_S (\bar{\mathbf{E}} \times \bar{\mathbf{H}}^*) \cdot d\bar{\mathbf{s}} + \\ \frac{1}{2}\iiint_V (\sigma' + \omega\epsilon'')E^2 + \omega\mu''H^2 dv + \\ j2\omega \left[\iiint_V \frac{1}{4}\mu'H^2 dv - \iiint_V \frac{1}{4}\left(\epsilon' - \frac{\sigma'}{\omega}\right)E^2 dv \right] \quad (2-2)$$

Each term in equation 2-2 can be identified. This yields the conservation of power equation:

$$P_s = P_e + P_d + j2\omega(\bar{W}_m - \bar{W}_e)$$

The complex power supplied by the sources is

$$P_s = -\frac{1}{2}\iiint_V \bar{\mathbf{M}}_a \cdot \bar{\mathbf{H}}^* + \bar{\mathbf{E}} \cdot \bar{\mathbf{J}}_a^* dv$$

The complex power exiting the volume is

$$P_e = \frac{1}{2}\oint_S (\bar{\mathbf{E}} \times \bar{\mathbf{H}}^*) \cdot d\bar{\mathbf{s}}$$

The real power being dissipated in the volume is

$$P_d = \frac{1}{2}\iiint_V (\sigma' + \omega\epsilon'')E^2 + \omega\mu''H^2 dv \quad (2-3)$$

The time averaged stored magnetic energy in the volume is

$$\bar{W}_m = \iiint_V \frac{1}{4}\mu'H^2 dv$$

And finally, the time averaged stored electric energy in the volume is

$$\bar{W}_e = \iiint_V \frac{1}{4}\left(\epsilon' - \frac{\sigma'}{\omega}\right)E^2 dv$$

A subtle point about equation 2-3 should be emphasized: it is necessary to calculate the total E and the total H in each region and use them in the equation. In the case of plane waves, it is tempting to use the power densities in the incident, reflected and transmitted waves to calculate the power absorbed. However, this leads to erroneous results. A simple example will serve to illustrate this. Consider a plane wave normally incident on a boundary as shown in Fig. 2-2. The wave reflects from the boundary with some reflection coefficient Γ . The incident electric field can be expressed as

$$\bar{E}_i = \hat{z}E_0 e^{-\gamma y}$$

where $\gamma = \alpha + j\beta$ is the propagation constant with α the attenuation constant in Nepers per meter, β the phase constant in radians per meter and E_0 the field strength. Thus, the power density in the incident plane wave is

$$\bar{P}_i = \frac{1}{2} \bar{E}_i \times \bar{H}_i^* = \hat{y} \frac{|E_0|^2}{2\eta^*} e^{-2\alpha y}$$

The power density in the reflected plane wave is

$$\bar{P}_r = \frac{1}{2} \bar{E}_r \times \bar{H}_r^* = -\hat{y} \frac{|\Gamma E_0|^2}{2\eta^*} e^{2\alpha y}$$

Thus it is tempting to say that the total power density on the incident side is just the sum of these two:

$$\bar{P}_t = \hat{y} \frac{|E_0|^2}{2\eta^*} \left(e^{-2\alpha y} - |\Gamma|^2 e^{2\alpha y} \right) \quad (2-4)$$

This is, however, wrong.

The total electric field on the incident side is

$$\bar{E}_t = \bar{E}_i + \bar{E}_r = \hat{z}E_0 \left(e^{-\gamma y} + \Gamma e^{\gamma y} \right)$$

The total magnetic field on the incident side is

$$\bar{H}_t = \bar{H}_i + \bar{H}_r = \hat{x} \frac{E_0}{\eta} \left(e^{-\gamma y} - \Gamma e^{\gamma y} \right)$$

Thus the total power density on the incident side is

$$\bar{P}_t = \frac{1}{2} \bar{E}_t \times \bar{H}_t^* = \hat{y} \frac{|E_0|^2}{2\eta^*} \left(e^{-2\alpha y} + 2j \text{Im} \left\{ \Gamma e^{j2\beta y} \right\} - |\Gamma|^2 e^{2\alpha y} \right) \quad (2-5)$$

Comparison of equations 2-4 and 2-5 reveals a missing term in equation 2-4. This term is important in that it maintains the conservation of power for all the fields in this example. (Note that this missing term does not contribute to the time-averaged power flow because the time averaging involves only the

real part of the right-hand side of equation 2-5.) Therefore, in Section 3, where plane waves incident on a planar absorber are considered, rather than differencing the incident and scattered fields to obtain the power dissipated, as has been done previously, P_d will be calculated through the integral indicated in equation 2-3.

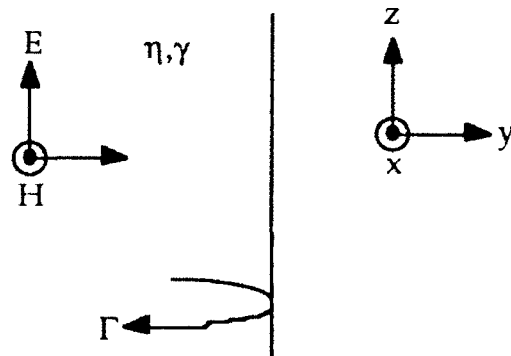


Fig. 2-2 A plane wave normally incident on a boundary between
2 materials

2.2.2 Physical Interpretation of Complex Material Parameters

As stated at the beginning of Section 2.2.1, the electromagnetic material parameters are, in general, complex values. The physical interpretation of these complex values will now be discussed.

2.2.2.1 Polarization Loss

The electric flux density D is related to the electric field E and the polarization P_e as

$$\vec{D} = \epsilon_0 \vec{E} + \vec{P}_e$$

For a linear material, the polarization is linearly dependent on the electric field as

$$\vec{P}_e = \epsilon_0 \chi_e \vec{E}$$

where χ_e , a dimensionless quantity, is the electric susceptibility. Thus, the electric flux density is related to the electric field as

$$\vec{D} = \epsilon_0 (1 + \chi_e) \vec{E} = \epsilon \vec{E}$$

Thus, the permittivity of the material is

$$\epsilon = \epsilon' - j\epsilon'' = \epsilon_0 (1 + \chi_e)$$

Because ϵ_0 is a real-valued constant, χ_e must be complex if $\epsilon'' \neq 0$. Therefore, the polarization is dependent on the electric field in a complex manner.

A complex relationship between two quantities implies a magnitude and phase difference. Therefore, the polarization must be out of phase with an applied electric field when $\epsilon'' \neq 0$. From equation 2-3, it can be seen that the term $\sigma + \omega\epsilon''$ is a loss term. King refers to this quantity as the "effective conductivity" [2]. Thus, the imaginary part of permittivity leads to heating of a material. Summarizing, when the permittivity of the material is complex, the polarization is out of phase with the electric field and heat is generated in the material.

A physical understanding of how the imaginary part of permittivity is similar to conductivity can be gained by considering an electric field applied to a polarizable material. Consider an infinite sheet of a polarizable material in the presence of a uniform, time varying, single frequency electric field, as shown in Fig. 2-3. At some moment of time, the electric field is maximum and the charges are distributed as shown in Fig. 2-3a. Allowing for some phase lag, at some time later the polarization has reached a maximum and the charges are as shown in Fig. 2-3b. At this moment, however, the electric field has changed from that in Fig. 2-3a. After half a period of time has elapsed from Fig. 2-3a, the electric field is maximum in the opposite direction. The charges have begun to realign with the electric field, but lag somewhat behind, as shown in Fig. 2-3c. Again, allowing for some phase lag, at some time later, the polarization has reached a maximum in the opposite direction from Fig. 2-3b and the charges are as shown in Fig. 2-3d. The net effect is that charges are in motion. These charges in motion are equivalent to a current. Thus, the polarizable nature of the material has led to a "displacement current". This current will track in phase with the electric field in a material whose permittivity is entirely real, however, the phase lag in a material with complex permittivity indicates that loss is occurring.

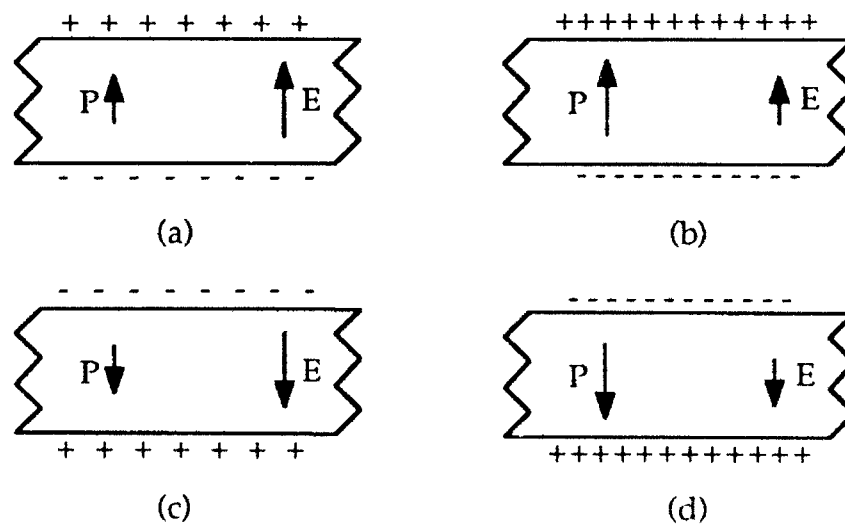


Fig. 2-3 Polarization of a dielectric sheet

2.2.2.2 Magnetization Loss

The magnetic flux density \vec{B} is related to the magnetic field \vec{H} and the magnetization \vec{P}_m as

$$\vec{B} = \mu_0(\vec{H} + \vec{P}_m)$$

For a linear material, the magnetization is linearly dependent on the magnetic field as

$$\vec{P}_m = \chi_m \vec{H}$$

where χ_m , a dimensionless quantity, is the magnetic susceptibility. Thus, the magnetic flux density is related to the magnetic field as

$$\vec{B} = \mu_0(1 + \chi_m)\vec{H} = \mu\vec{H}$$

Thus, the permeability of the material is

$$\mu = \mu' - j\mu'' = \mu_0(1 + \chi_m)$$

Because μ_0 is a real-valued constant, χ_m must be complex if $\mu'' \neq 0$.

Therefore, the magnetization is dependent on the magnetic field in a complex manner.

From equation 2-3, it can be seen that the term μ'' is also a loss term. Thus, we have come to the same point as in the discussion of the electric field. Although an illustrative example showing the physical explanation of loss due to complex permeability would be somewhat more complex than that for permittivity, the conclusion would be the same, namely, the imaginary part of permeability results in a phase lag between the magnetic field and the magnetization which leads to heating of the material.

2.2.2.3 Conduction Loss

The conduction current in a material is related to the electric field as

$$\vec{J} = \sigma\vec{E}$$

The conductivity is allowed to be complex for generality, thus

$$\sigma = \sigma' - j\sigma''$$

This indicates that the conduction current can have a different phase from the electric field in a material where $\sigma'' \neq 0$. This is not the case for the type of materials considered in this work. However, there are some materials which exhibit complex conductivity, plasmas for example.

The materials of interest in this work will typically have complex permittivities, real permeabilities and real conductivities. Equation 2-3 shows that the two parts of "effective conductivity", σ and $\omega\epsilon''$ are indistinguishable

as far as their effects on the absorbed power. At DC only σ affects the absorbed power. At high frequencies most of the effective conductivity is derived from $\omega\epsilon''$. In addition, it is possible to use an effective conductivity which groups all the electrical loss into σ or an imaginary permittivity which groups all the electrical loss into $\omega\epsilon''$. Some of the analyses used in this work use σ while others use $\omega\epsilon''$; the form chosen is that which seems most appropriate to the topic of discussion. For example, the measurement of material parameters at high frequencies outlined in Section 4 develops equations based on ϵ'' . Thus the electrical loss at high frequencies is entirely modeled by ϵ'' . Section 4 develops the DC material measurement on the basis of σ . To add σ to the $\omega\epsilon''$ term at high frequencies is not allowable because the $\omega\epsilon''$ term already contains all the lossy characteristics.

2.2.3 Power Absorbed Related to Field Orientation

From the previous work, the power dissipated in a volume due to the existing electromagnetic fields in that volume is

$$P_d = \frac{1}{2} \iiint_V (\sigma + \omega\epsilon'') E^2 + \omega\mu'' H^2 dv$$

Consider the geometry of a semi-infinite slab of absorber with air on either side, as shown in Fig. 2-4. It is preferable to talk of the power absorbed, P_{abs} , per square meter (W/m^2) in the tangential plane. Thus,

$$P_{abs} = \frac{1}{2} \int_0^d (\sigma + \omega\epsilon'') E^2 + \omega\mu'' H^2 dn \quad (2-6)$$

where n is the dimension normal to the boundary.

Two simplifying assumptions are now made. First, it is assumed that the absorber thickness d is very small, much less than a wavelength. Second, it is assumed that the material parameters are such that the absorption is small. As a result of these assumptions, the fields in the absorber can be approximated as constants in n .

The boundary conditions require that the tangential components of E and H be continuous at both boundaries. From the thin, low-loss assumptions above, it is possible to consider all tangential E components to be approximately equal. Thus,

$$E_{t1} = E_{t2} = E_{t3} = E_t$$

where the subscript refers to the region in which the tangential component exists. The same applies to the tangential H components. Thus,

$$H_{t1} = H_{t2} = H_{t3} = H_t$$

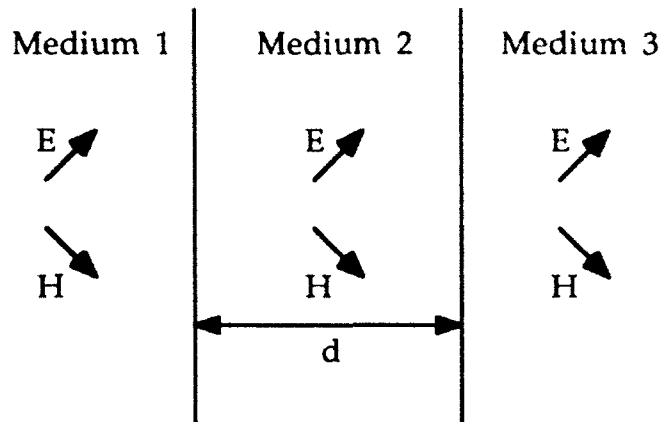


Fig. 2-4 Electromagnetic fields in three regions

The boundary conditions also require that the normal components of D and B be continuous at both boundaries. The thin, low-loss assumptions allow the normal D components in all regions to be considered approximately equal. Thus,

$$D_{n1} = D_{n2} = D_{n3}$$

Expressed in terms of E in each region this is

$$\epsilon_1 E_{n1} = \epsilon_2 E_{n2} = \epsilon_3 E_{n3}$$

If regions 1 and 3 are both vacuum (or air) then this can be rewritten as

$$E_{n1} = \frac{\epsilon_2}{\epsilon_0} E_{n2} = E_{n3} = E_n$$

Thus, the normal component of the electric field in region 2 can be approximated as

$$E_{n2} = E_n \frac{\epsilon_0}{\epsilon_2}$$

Similarly, continuity of the normal component of B yields

$$H_{n2} = H_n \frac{\mu_0}{\mu_2}$$

Substituting each of the above components into equation 2-6 and assuming that the fields do not vary appreciably in n , then the total power absorbed per square meter in region 2 is

$$P_{abs} = \frac{d}{2} \left[(\sigma' + \omega\epsilon'') \left(E_t^2 + E_n^2 \left| \frac{\epsilon_0}{\epsilon_2} \right|^2 \right) + \omega\mu'' \left(H_t^2 + H_n^2 \left| \frac{\mu_0}{\mu_2} \right|^2 \right) \right]$$

This demonstrates that the power absorbed from the normal E and the normal H field components is reduced by the square of the relative permittivity and permeability of the absorber material.

Consider an absorbing screen which is designed to heat from the

electric field. Most electric field absorbers are likely to have $\epsilon_r \geq 3$ or 4. Thus, the heating due to the normal component of E will be at least an order of magnitude less than that due to the tangential components.

Therefore, it is apparent that the heating of a thin, low-loss, absorbing screen will be predominantly from tangential field components.

The amount of heating which arises from a plane wave normally incident on a semi-infinite absorbing sheet will be considered in Section 3. This particular form of field structure will be used to design an absorber with optimum properties.

3 Design of an Absorbing Screen

The typical configuration used for measuring electric fields by thermographic mapping includes a thin sheet of absorbing material. The design objectives for this material are that it exhibit a significant heat rise for a small amount of incident electromagnetic energy and that it not disturb the fields which it is measuring. These two objectives are, in general, in opposition. Design of an absorber involves a trade-off between these two desirable properties.

In order to adequately understand the trade-offs in the design of an absorber, it is desirable to be able to predict the response of the absorber in some situation simple enough to allow for a closed-form analysis. One such configuration is that of a linearly polarized plane wave incident on a semi-infinite sheet of absorber. This configuration will be analyzed for a general case and then reduced to the case of normal incidence. The results from the normal incidence analysis will be used to evaluate the effects of the absorber properties on the heat generated in the absorber and the amount of field disturbance.

3.1 Plane Waves Incident on an Absorbing Screen

The geometry to be considered is shown in Fig. 3-1. The incident plane wave is linearly polarized. In order to allow for generality in the model, both parallel and perpendicular polarizations (with respect to the plane of incidence) will be examined. These two cases yield the same results if the angle of incidence is reduced to 0 (normal incidence). The incident wave

consisting of \bar{E}_1^+ and \bar{H}_1^+ reflects at the $y=0$ boundary giving rise to \bar{E}_1^- and \bar{H}_1^- ;

it also transmits through the boundary giving rise to \bar{E}_2^+ and \bar{H}_2^+ . This plane

wave reflects at the $y=d$ boundary giving rise to \vec{E}_2^- and \vec{H}_2^- ; it also transmits through the boundary as \vec{E}_3 and \vec{H}_3 . It is assumed that the incident field strength and angle of incidence are known. The solution for the unknown fields and angles will be found in the frequency domain.

3.1.1 Parallel Polarization

The geometry for parallel polarization is shown in Fig. 3-2. The characteristic impedance and propagation constant of a region are given as

$$\eta = \sqrt{\frac{j\omega\mu}{\sigma + j\omega\epsilon}}$$

$$\gamma = j\omega\sqrt{\mu\epsilon}\sqrt{1 + \frac{\sigma}{j\omega\epsilon}} = \alpha + j\beta$$

The general forms for the electric and magnetic fields are

$$\vec{E}_1^+ = E_1^+(-\hat{y}\sin\theta_1 + \hat{z}\cos\theta_1)e^{-j\beta_1(y\cos\theta_1 + z\sin\theta_1)}$$

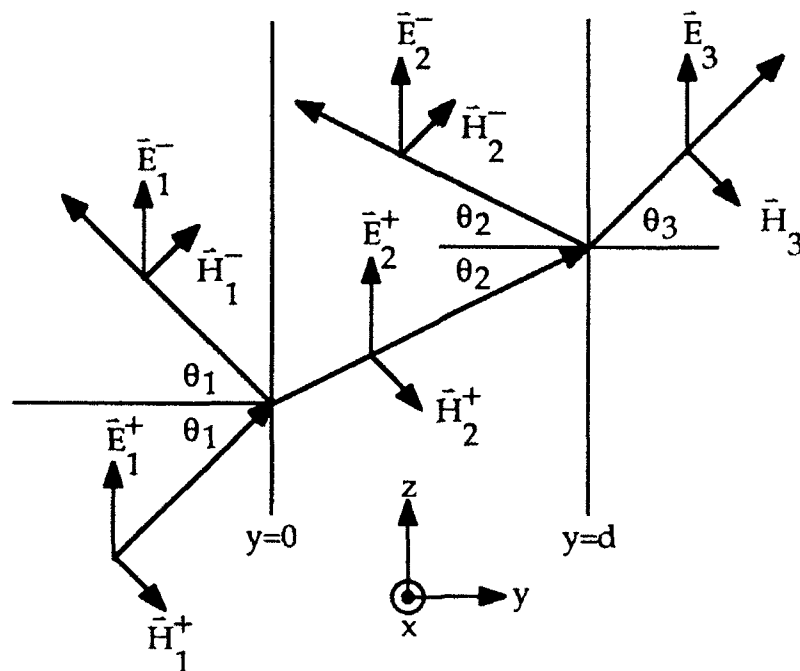


Fig. 3-1 A general plane wave in a planar 3-region geometry

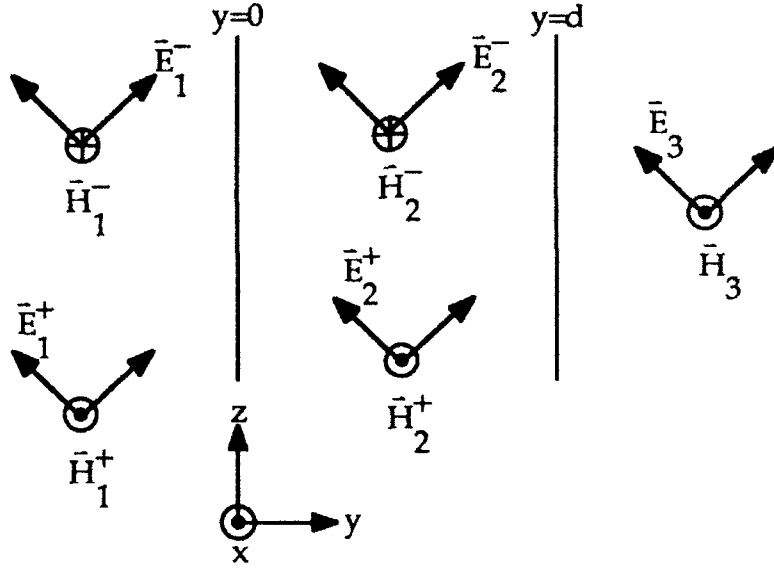


Fig. 3-2 A parallel polarized plane wave in a planar 3-region geometry

$$\begin{aligned} \bar{H}_1^+ &= \frac{E_1^+}{\eta_1} \hat{x} e^{-j\beta_1(y \cos\theta_1 + z \sin\theta_1)} \\ \bar{E}_1^- &= E_1^- (\hat{y} \sin\theta_1 + \hat{z} \cos\theta_1) e^{-j\beta_1(-y \cos\theta_1 + z \sin\theta_1)} \\ \bar{H}_1^- &= -\frac{E_1^-}{\eta_1} \hat{x} e^{-j\beta_1(-y \cos\theta_1 + z \sin\theta_1)} \\ \bar{E}_2^+ &= E_2^+ (-\hat{y} \sin\theta_2 + \hat{z} \cos\theta_2) e^{-\gamma_2(y \cos\theta_2 + z \sin\theta_2)} \\ \bar{H}_2^+ &= \frac{E_2^+}{\eta_2} \hat{x} e^{-\gamma_2(y \cos\theta_2 + z \sin\theta_2)} \\ \bar{E}_2^- &= E_2^- (\hat{y} \sin\theta_2 + \hat{z} \cos\theta_2) e^{-\gamma_2(-y \cos\theta_2 + z \sin\theta_2)} \\ \bar{H}_2^- &= -\frac{E_2^-}{\eta_2} \hat{x} e^{-\gamma_2(-y \cos\theta_2 + z \sin\theta_2)} \\ \bar{E}_3 &= E_3 (-\hat{y} \sin\theta_3 + \hat{z} \cos\theta_3) e^{-j\beta_3((y-d) \cos\theta_3 + z \sin\theta_3)} \end{aligned}$$

$$\bar{H}_3 = \frac{E_3}{\eta_3} \hat{x} e^{-j\beta_3((y-d)\cos\theta_3 + z\sin\theta_3)}$$

In these forms of the fields, regions 1 and 3 are assumed to be lossless. Furthermore, it is assumed that regions 1 and 3 are air or vacuum, thus, the intrinsic impedances and propagation constants in those two regions are denoted by η_0 and $j\beta_0$.

Snell's law fixes the relationship between the angles as

$$\frac{\sin\theta_1}{\sin\theta_2} = \frac{\gamma_2}{j\beta_0}$$

and also

$$\theta_1 = \theta_3$$

Continuity of the field components parallel to the interfaces yields four boundary conditions:

$$\begin{aligned} & \left[E_{1z}^+ + E_{1z}^- = E_{2z}^+ + E_{2z}^- \right]_{y=0, z=0} \\ & \left[H_{1x}^+ + H_{1x}^- = H_{2x}^+ + H_{2x}^- \right]_{y=0, z=0} \\ & \left[E_{2z}^+ + E_{2z}^- = E_{3z} \right]_{y=d, z=0} \\ & \left[H_{2x}^+ + H_{2x}^- = H_{3x} \right]_{y=d, z=0} \end{aligned}$$

These four conditions are adequate to determine E_1^- , E_2^+ , E_2^- and E_3 in terms

of E_1^+ :

$$\begin{aligned} E_1^- &= E_1^+ \frac{\Gamma(1-P^2)}{1-\Gamma^2 P^2} \\ E_2^+ &= E_1^+ \frac{\Gamma+1}{1-\Gamma^2 P^2} \\ E_2^- &= E_1^+ \frac{-\Gamma P^2(\Gamma+1)}{1-\Gamma^2 P^2} \end{aligned}$$

$$E_3 = E_1^+ \frac{P(1-\Gamma^2)}{1-\Gamma^2 P^2}$$

where:

$$\Gamma = \frac{\eta_2 \cos\theta_2 - \eta_0 \cos\theta_1}{\eta_2 \cos\theta_2 + \eta_0 \cos\theta_1}$$

$$P = e^{-\gamma_2 d \cos\theta_2}$$

3.1.2 Perpendicular Polarization

The geometry for perpendicular polarization is shown in Fig. 3-3.

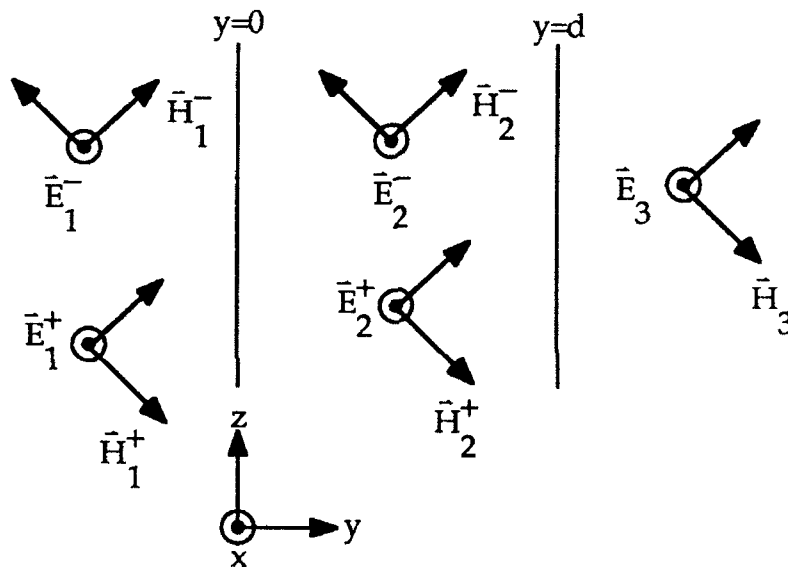


Fig. 3-3 A perpendicularly polarized plane wave in a planar 3-region geometry

The general forms for the electric and magnetic fields in this case are given as

$$\tilde{E}_1^+ = E_1^+ \hat{x} e^{-j\beta_1(y \cos\theta_1 + z \sin\theta_1)}$$

$$\tilde{H}_1^+ = \frac{E_1^+}{\eta_1} (\hat{y} \sin\theta_1 - \hat{z} \cos\theta_1) e^{-j\beta_1(y \cos\theta_1 + z \sin\theta_1)}$$

$$\begin{aligned}\bar{E}_1^- &= E_1^- \hat{x} e^{-j\beta_1(-y \cos\theta_1 + z \sin\theta_1)} \\ \bar{H}_1^- &= \frac{E_1^-}{\eta_1} (\hat{y} \sin\theta_1 + \hat{z} \cos\theta_1) e^{-j\beta_1(-y \cos\theta_1 + z \sin\theta_1)} \\ \bar{E}_2^+ &= E_2^+ \hat{x} e^{-\gamma_2(y \cos\theta_2 + z \sin\theta_2)} \\ \bar{H}_2^+ &= \frac{E_2^+}{\eta_2} (\hat{y} \sin\theta_2 - \hat{z} \cos\theta_2) e^{-\gamma_2(y \cos\theta_2 + z \sin\theta_2)} \\ \bar{E}_2^- &= E_2^- \hat{x} e^{-\gamma_2(-y \cos\theta_2 + z \sin\theta_2)} \\ \bar{H}_2^- &= \frac{E_2^-}{\eta_2} (\hat{y} \sin\theta_2 + \hat{z} \cos\theta_2) e^{-\gamma_2(-y \cos\theta_2 + z \sin\theta_2)} \\ \bar{E}_3 &= E_3 \hat{x} e^{-j\beta_3((y-d) \cos\theta_3 + z \sin\theta_3)} \\ \bar{H}_3 &= \frac{E_3}{\eta_3} (\hat{y} \sin\theta_3 - \hat{z} \cos\theta_3) e^{-j\beta_3((y-d) \cos\theta_3 + z \sin\theta_3)}\end{aligned}$$

As before, Snell's law fixes the relationship between the angles as

$$\frac{\sin\theta_1}{\sin\theta_2} = \frac{\gamma_2}{j\beta_0}$$

and also

$$\theta_1 = \theta_3$$

Again, continuity of the field components parallel to the interfaces yields four boundary conditions:

$$\begin{aligned}\left[E_{1x}^+ + E_{1x}^- = E_{2x}^+ + E_{2x}^- \right]_{y=0, z=0} \\ \left[H_{1z}^+ + H_{1z}^- = H_{2z}^+ + H_{2z}^- \right]_{y=0, z=0} \\ \left[E_{2x}^+ + E_{2x}^- = E_{3x} \right]_{y=d, z=0} \\ \left[H_{2z}^+ + H_{2z}^- = H_{3z} \right]_{y=d, z=0}\end{aligned}$$

These four conditions are adequate to determine E_1^- , E_2^+ , E_2^- and E_3 in terms

of E_1^+ :

$$E_1^- = E_1^+ \frac{\Gamma(1-P^2)}{1-\Gamma^2 P^2}$$

$$E_2^+ = E_1^+ \frac{\Gamma+1}{1-\Gamma^2 P^2}$$

$$E_2^- = E_1^+ \frac{-\Gamma P^2(\Gamma+1)}{1-\Gamma^2 P^2}$$

$$E_3 = E_1^+ \frac{P(1-\Gamma^2)}{1-\Gamma^2 P^2}$$

where:

$$\Gamma = \frac{\eta_2 \cos\theta_1 - \eta_0 \cos\theta_2}{\eta_2 \cos\theta_1 + \eta_0 \cos\theta_2}$$

$$P = e^{-\gamma_2 d \cos\theta_2}$$

These are the same form of results as for the parallel polarization case except for a slight change in the Γ term.

3.1.3 Normal Incidence

At normal incidence all the incidence angles are zero. For this special case, the magnitudes of the resulting fields are as they were in the previous two cases. The parameters Γ and P become

$$\Gamma = \frac{\eta_2 - \eta_0}{\eta_2 + \eta_0}$$

$$P = e^{-\gamma_2 d}$$

3.2 Power Absorbed in the Screen

Due to the interaction of the plane wave and the sheet of lossy material, heat will be deposited in the material as described in Section 2. The total power in watts absorbed in the material was shown to be related to the electromagnetic field by the relation

$$P_d = \frac{1}{2} \iiint_V (\sigma' + \omega \epsilon'') E^2 + \omega \mu'' H^2 dv$$

For plane waves it is possible to perform the indicated integral to obtain a closed-form solution for P_d . Because the intermediate results may be useful, they will be given here as steps leading to the closed-form P_d . The plane wave is assumed to be normally incident.

The total electric field in the absorbing region is

$$\bar{E}_2 = \hat{x} \left[E_2^+ e^{-\gamma_2 y} + E_2^- e^{+\gamma_2 y} \right]$$

The magnitude squared of the electric field is

$$\left| E_2 \right|^2 = E_2^2 = \left| E_2^+ \right|^2 e^{-2\alpha_2 y} + \left| E_2^- \right|^2 e^{2\alpha_2 y} + 2 \operatorname{Re} \left\{ E_2^+ E_2^{-*} e^{-j2\beta_2 y} \right\}$$

Integration of this yields

$$\int_0^d \left| E_2 \right|^2 dy = \left[\frac{\left| E_2^- \right|^2}{2\alpha_2} \left(e^{2\alpha_2 d} - 1 \right) - \frac{\left| E_2^+ \right|^2}{2\alpha_2} \left(e^{-2\alpha_2 d} - 1 \right) + \frac{1}{\beta_2} \operatorname{Re} \left\{ E_2^+ E_2^{-*} j \left(e^{-j2\beta_2 d} - 1 \right) \right\} \right]$$

The total magnetic field in the absorbing region is

$$\bar{H}_2 = \hat{z} \left[-\frac{E_2^+}{\eta_2} e^{-\gamma_2 y} + \frac{E_2^-}{\eta_2} e^{+\gamma_2 y} \right]$$

The magnitude squared of the magnetic field is

$$\left| H_2 \right|^2 = H_2^2 = \frac{\left[\left| E_2^+ \right|^2 e^{-2\alpha_2 y} + \left| E_2^- \right|^2 e^{2\alpha_2 y} - 2 \operatorname{Re} \left\{ E_2^+ E_2^{-*} e^{-j2\beta_2 y} \right\} \right]}{\left| \eta_2 \right|^2}$$

Integration of this yields

$$\int_0^d |H_2|^2 dy = \frac{\left[\frac{|E_2^-|^2}{2\alpha_2} (e^{2\alpha_2 d} - 1) - \frac{|E_2^+|^2}{2\alpha_2} (e^{-2\alpha_2 d} - 1) - \frac{1}{\beta_2} \operatorname{Re} \left\{ E_2^+ E_2^{-*} j (e^{-j2\beta_2 d} - 1) \right\} \right]}{|\eta_2|^2}$$

The total power absorbed per square meter of the absorbing material is thus

$$P_{\text{abs}} = \frac{(\sigma + \omega\epsilon'')}{4} \left[\frac{|E_2^-|^2}{\alpha_2} (e^{2\alpha_2 d} - 1) - \frac{|E_2^+|^2}{\alpha_2} (e^{-2\alpha_2 d} - 1) + \frac{2}{\beta_2} \operatorname{Re} \left\{ E_2^+ E_2^{-*} j (e^{-j2\beta_2 d} - 1) \right\} \right] + \frac{\omega\mu''}{4|\eta_2|^2} \left[\frac{|E_2^-|^2}{\alpha_2} (e^{2\alpha_2 d} - 1) - \frac{|E_2^+|^2}{\alpha_2} (e^{-2\alpha_2 d} - 1) - \frac{2}{\beta_2} \operatorname{Re} \left\{ E_2^+ E_2^{-*} j (e^{-j2\beta_2 d} - 1) \right\} \right]$$

The baseline design for the screen has a relative permeability $\mu_r=1$, a relative permittivity $\epsilon_r=3$, a conductivity $\sigma=1 \text{ 1}/\Omega\text{m}$, a thickness $d=0.003 \text{ m}$ and an operating frequency of $f=3 \text{ GHz}$. The two absorber parameters which were most easily controllable were the thickness and the effective conductivity. The relative permeability and permittivity were less controllable.

In the following series of plots two of these parameters will be varied, while all others will stay at their baseline values. The plots were generated by the Mathematica listing shown in Appendix A.2. In these plots, the conductivity was used rather than the imaginary part of the relative permittivity since either of these parameters adequately model the loss term, as discussed in Section 2. An alternative method for calculations based on complex permeability and complex permittivity is given in the Mathematica listing in Appendix A.3.

In order to remove the effects of the power density of the incident plane wave on the calculations, the power absorbed will be expressed as a percentage of the incident power density, i.e.

$$\%P_{\text{abs}} = \frac{P_{\text{abs}}}{P_{\text{inc}}} \times 100\%$$

Fig. 3-4 shows the variation of $\%P_{\text{abs}}$ with varying thickness and conductivity of the screen. For a screen with a thickness of 4 cm and a conductivity of $1 (\Omega\text{m})^{-1}$, about 73% of the incoming planewave power can be transformed into heat in the screen. It should be noted, however, that as the material is made thicker, the surface temperature is reduced due to thermal conduction from the hot surface where the fields are more intense to the cool regions inside the material which have less intense fields. Because it is the surface temperature which is ultimately of interest, it is not practical to use thick materials.

Fig. 3-5 shows the variation of $\%P_{\text{abs}}$ with varying frequency and thickness. This Fig. shows that the absorber can be constructed to be reasonably insensitive to variations in frequency, a desirable feature. Fig. 3-6 shows the variation of $\%P_{\text{abs}}$ with varying relative permittivity and thickness. This shows a general insensitivity of power absorption with relative permittivity. Fig. 3-7 shows the variation of $\%P_{\text{abs}}$ with varying relative permittivity and frequency. Fig. 3-8 shows the variation of $\%P_{\text{abs}}$ with varying conductivity and frequency. Figs. 3-9 and 3-10 show the variation of $\%P_{\text{abs}}$ with varying thickness. The difference between the two figures is in the range of thicknesses considered.

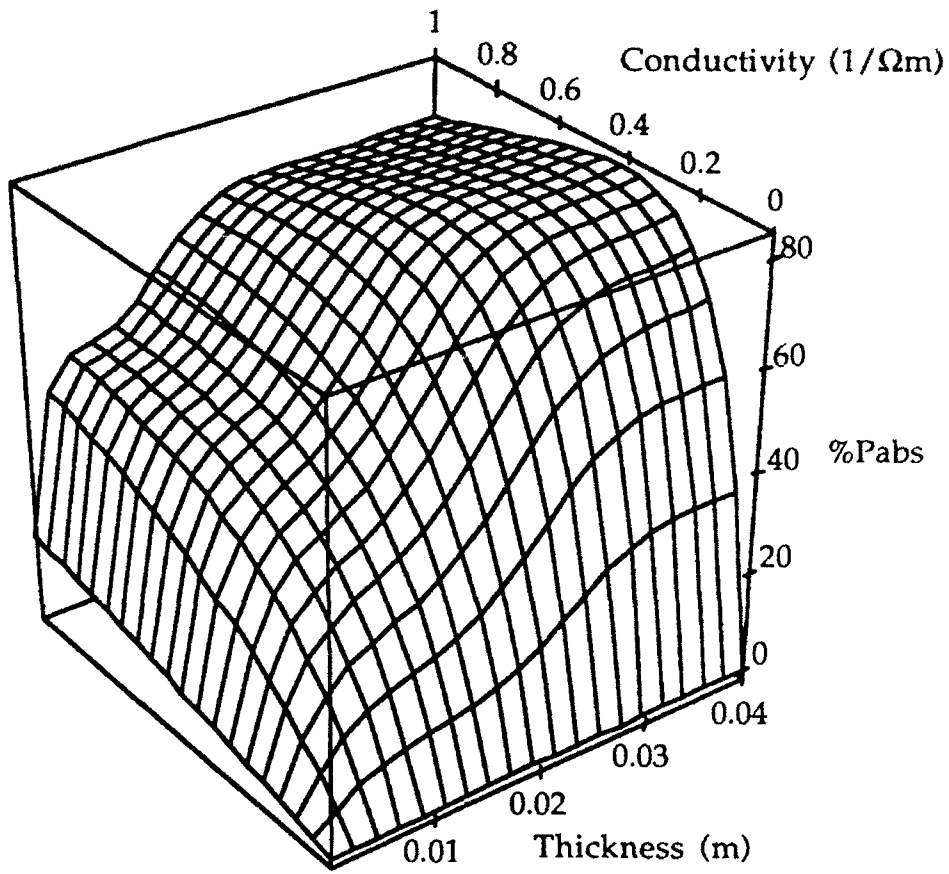


Fig. 3-4 %P_{abs} vs thickness and conductivity

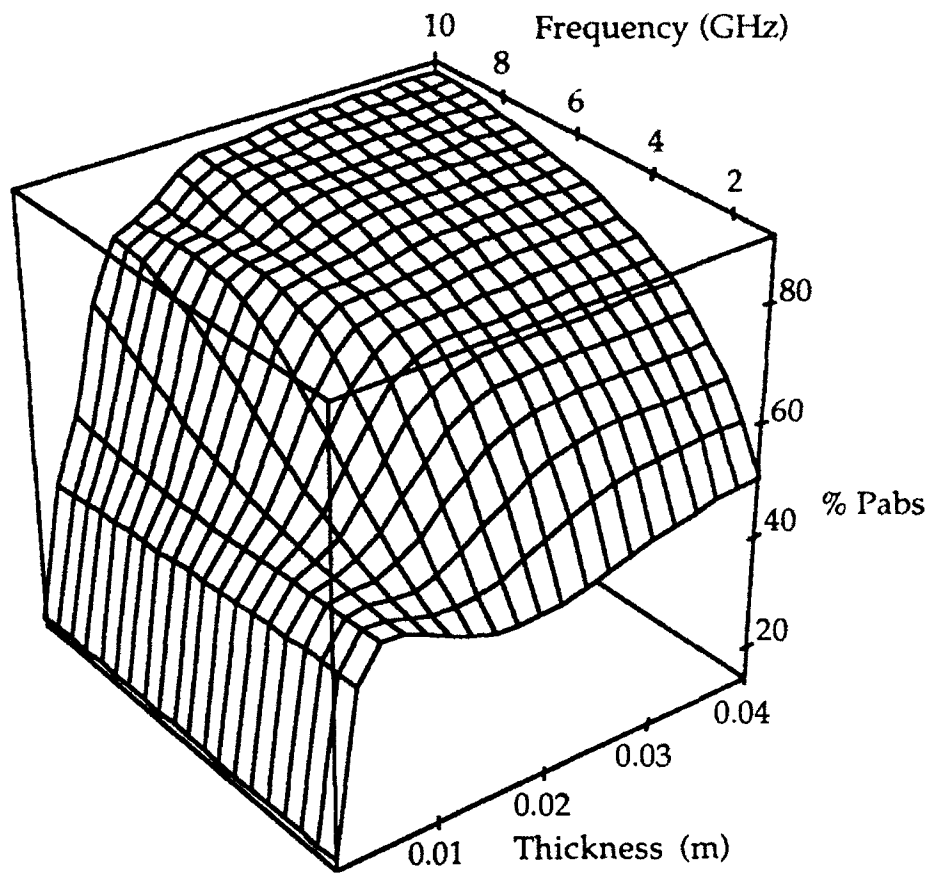


Fig. 3-5 %P_{abs} vs frequency and thickness

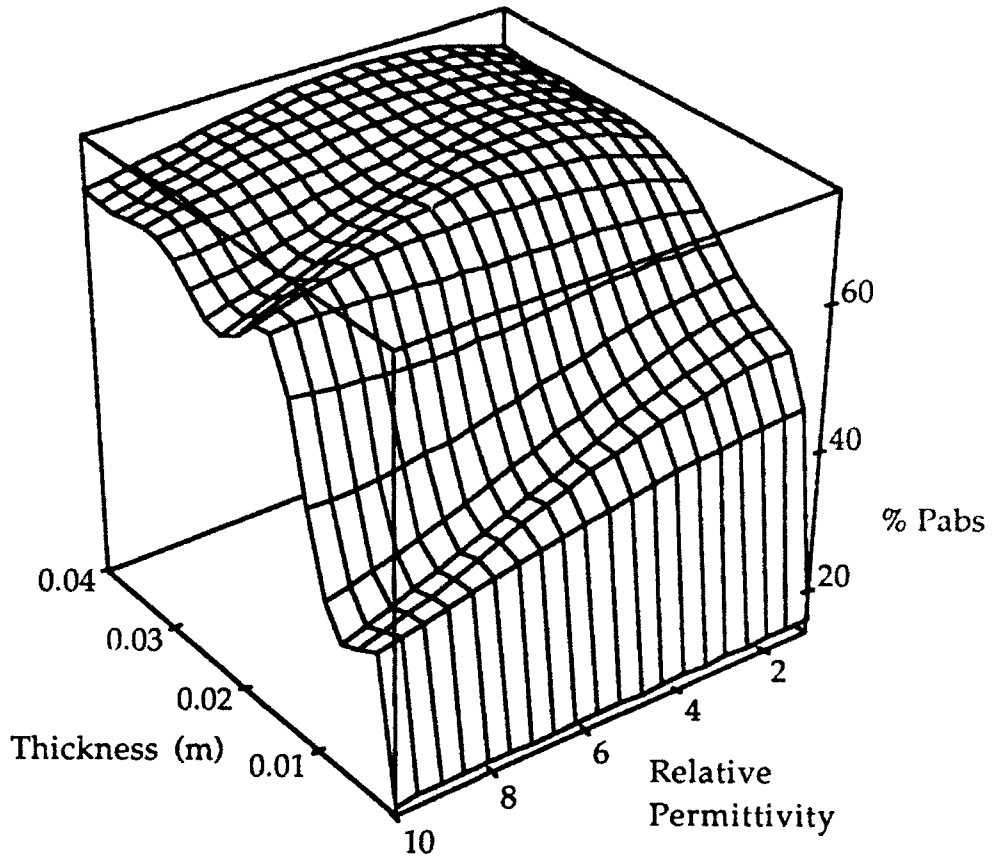


Fig. 3-6 $\%P_{abs}$ vs relative permittivity and thickness

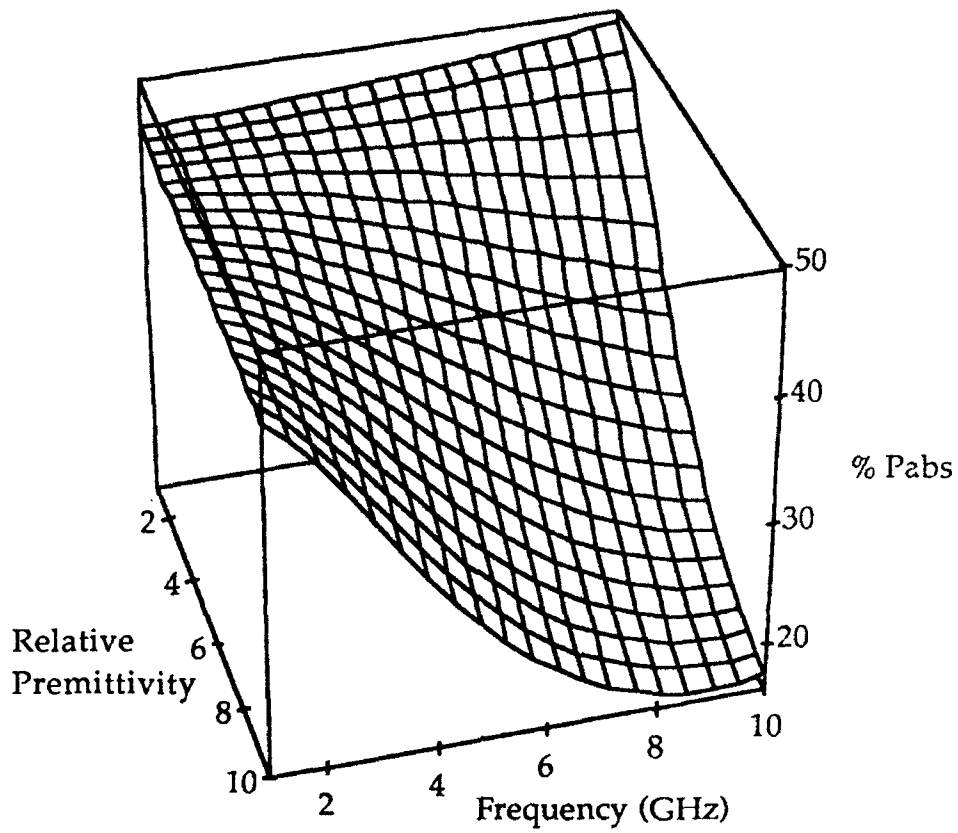


Fig. 3-7 %P_{abs} vs relative permittivity and frequency

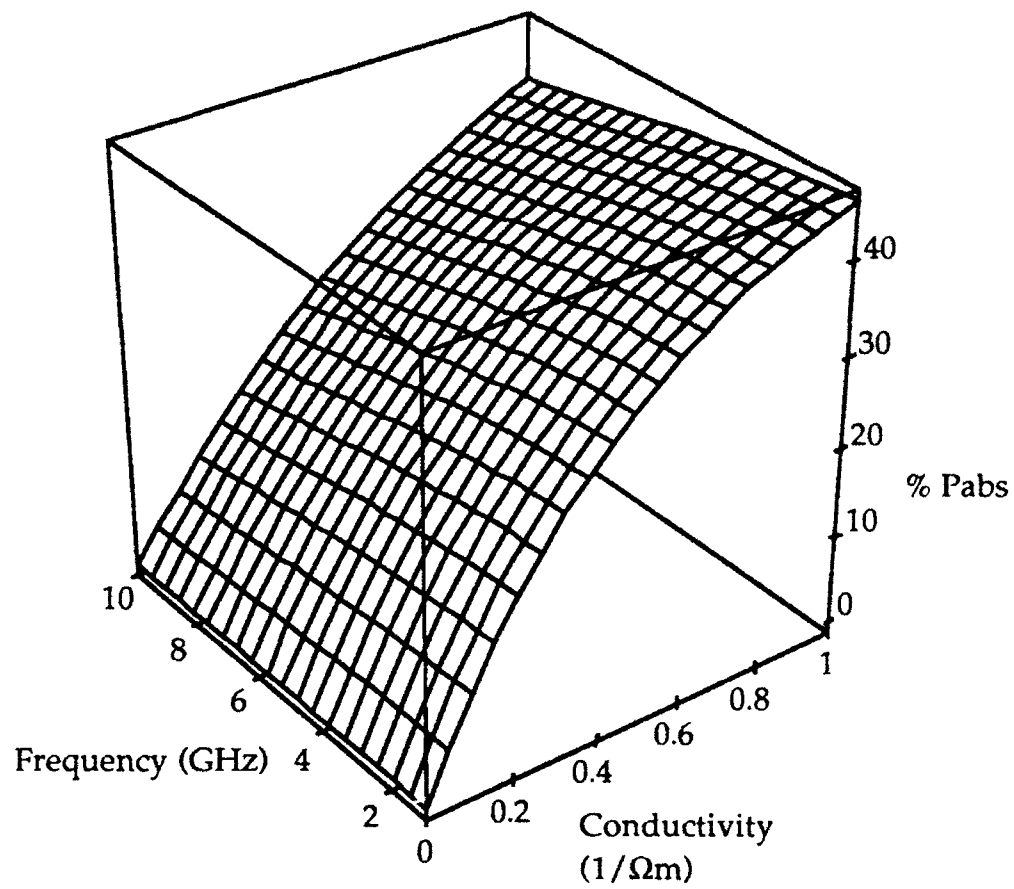


Fig. 3-8 %P_{abs} vs conductivity and frequency

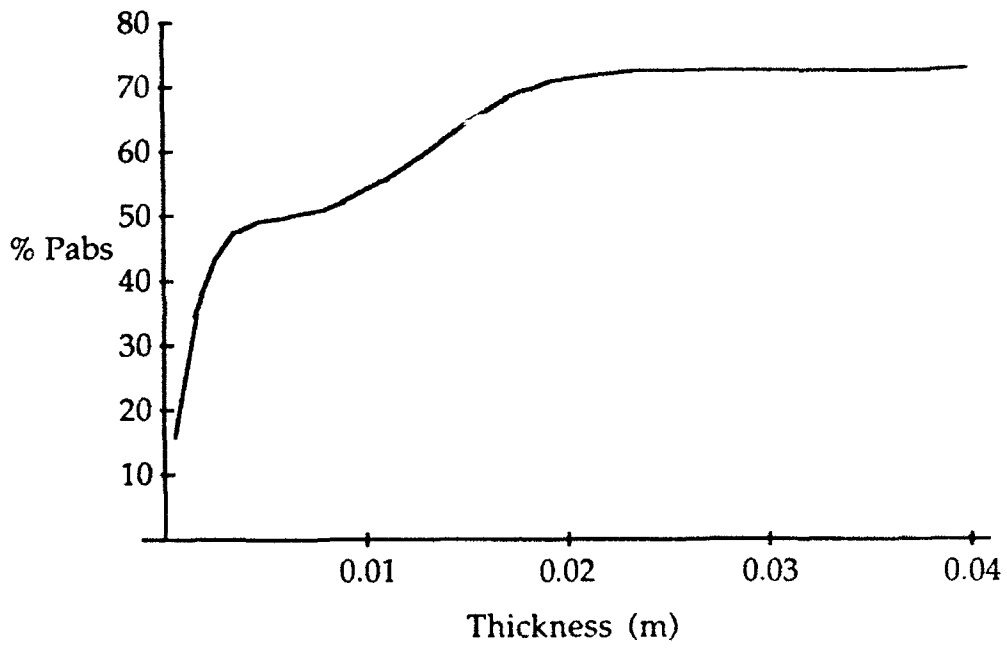


Fig. 3-9 %P_{abs} vs thickness

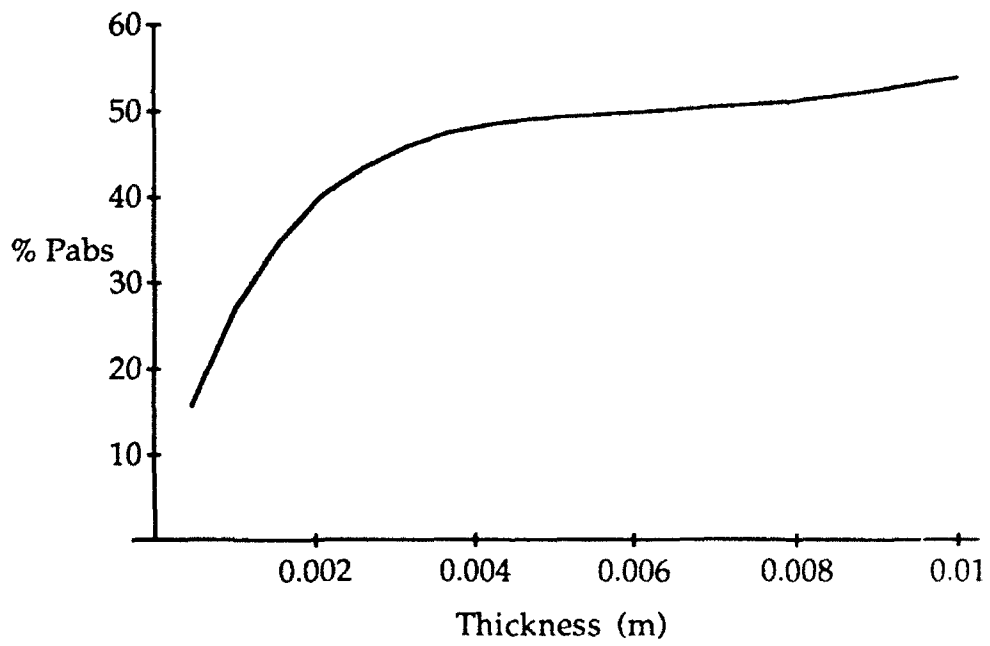


Fig. 3-10 %P_{abs} vs thickness for a thin absorber

3.3 Power Reflected by the Screen

Due to the mismatch between the intrinsic impedance of the air and the absorber material, some power will be reflected. The total reflected power in watts/m² is given as

$$P_{\text{refl}} = \frac{1}{2} \left(\bar{E}_1^- \times \bar{H}_1^{-*} \right) = \frac{|E_1^-|^2}{2\eta_0}$$

As with the power absorbed, power reflected will be expressed as a percentage of the incident power density, i.e.

$$\%P_{\text{refl}} = \frac{P_{\text{refl}}}{P_{\text{inc}}} \times 100\%$$

Fig. 3-11 shows the variation of %P_{refl} with varying thickness and conductivity. As the conductivity increases, the intrinsic impedance of the material is less well matched to free space and more of the incident wave is reflected. For an absorber with a thickness of 4 cm and a conductivity of 1 (Ωm)⁻¹, about 27% of the power is reflected. Together with the 73% power absorbed, this accounts for the power flow in the system.

Fig. 3-12 shows the variation of %P_{refl} with varying relative permittivity and thickness. Figs. 3-13 and 3-14 show the variation of %P_{refl} with varying thickness.

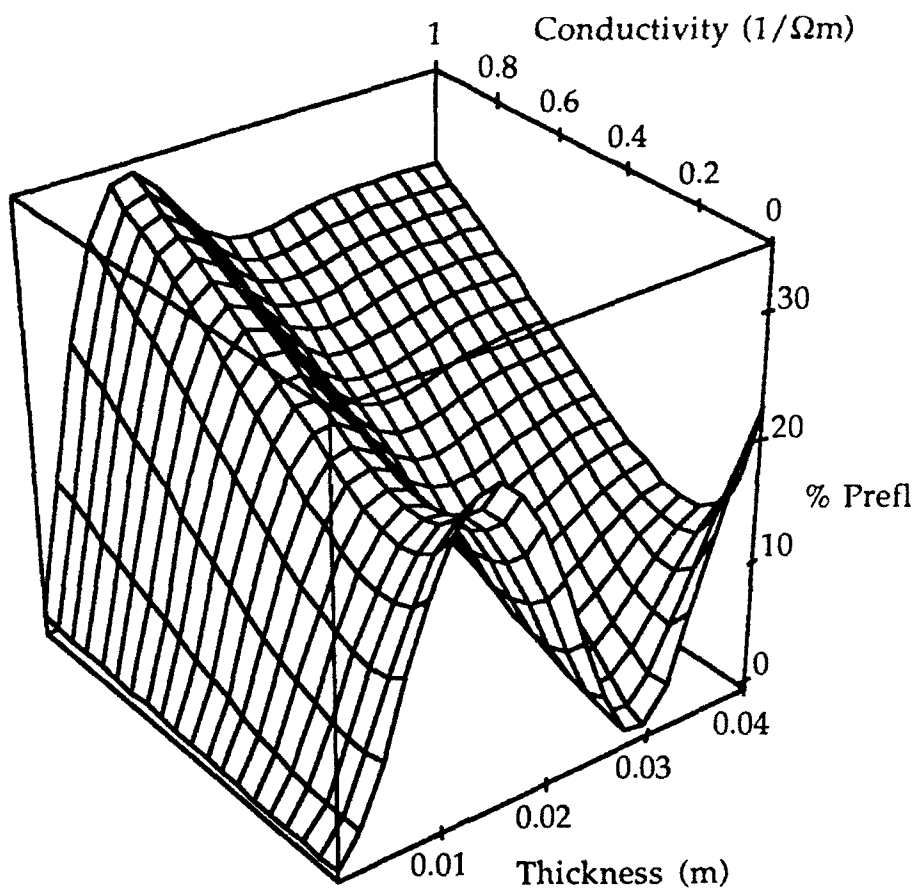


Fig. 3-11 %P_{refl} vs thickness and conductivity

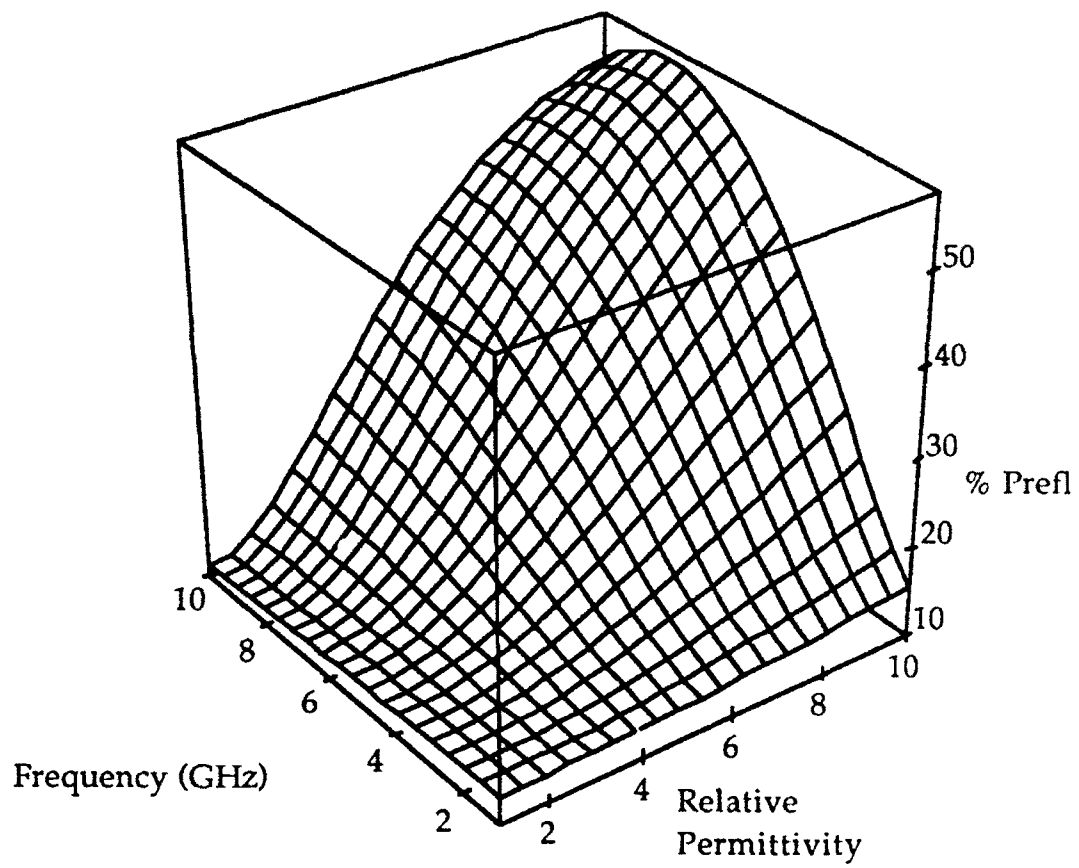


Fig. 3-12 $\%P_{\text{refl}}$ vs relative permittivity and frequency

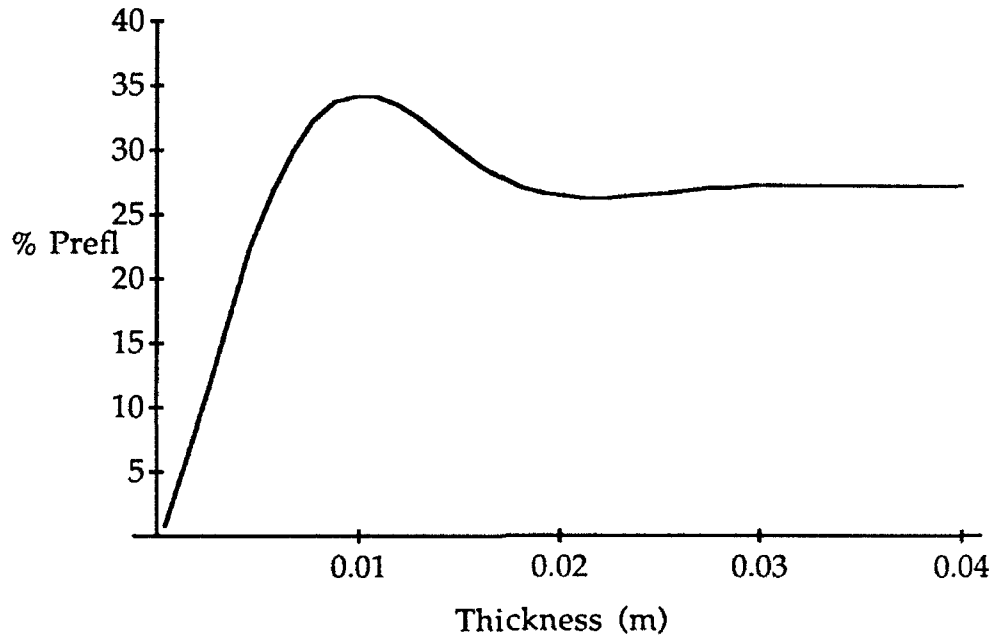


Fig. 3-13 %P_{refl} vs thickness

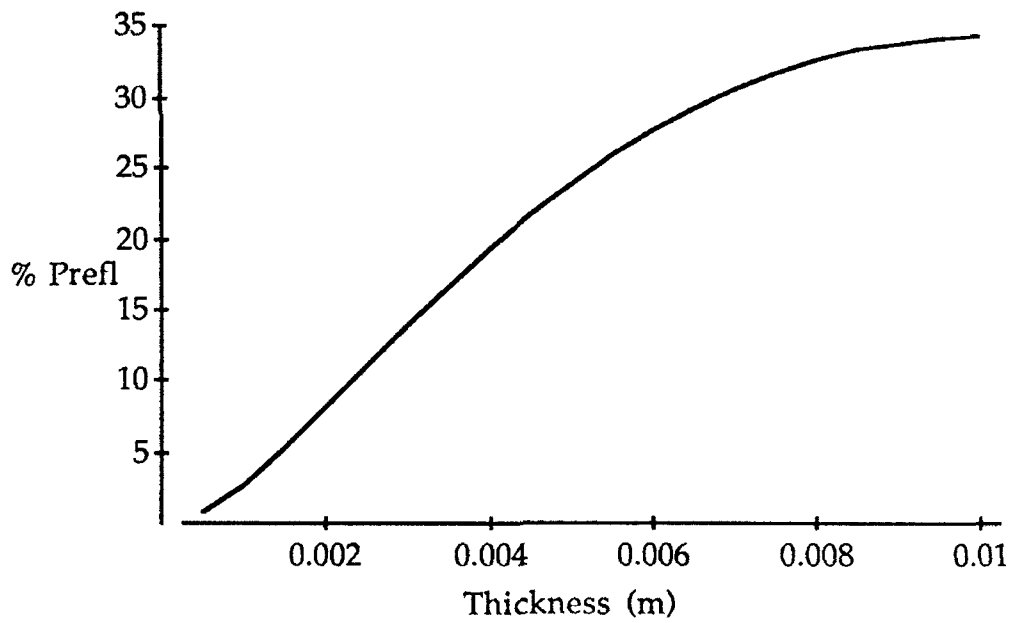


Fig. 3-14 %P_{refl} vs thickness for a thin absorber

3.4 The Ratio of Absorbed and Reflected Power

It is generally desirable that the screen absorb much more power than it

reflects. The effects of thickness and conductivity on the ratio of $\%P_{\text{abs}}/\%P_{\text{refl}}$ are shown in Fig. 3-15. The peak is due to a local minimum in P_{refl} . Figs. 3-16 and 3-17 show the variation of $\%P_{\text{abs}}/\%P_{\text{refl}}$ with varying thickness. The only difference between the two figures is in the range of thicknesses considered.

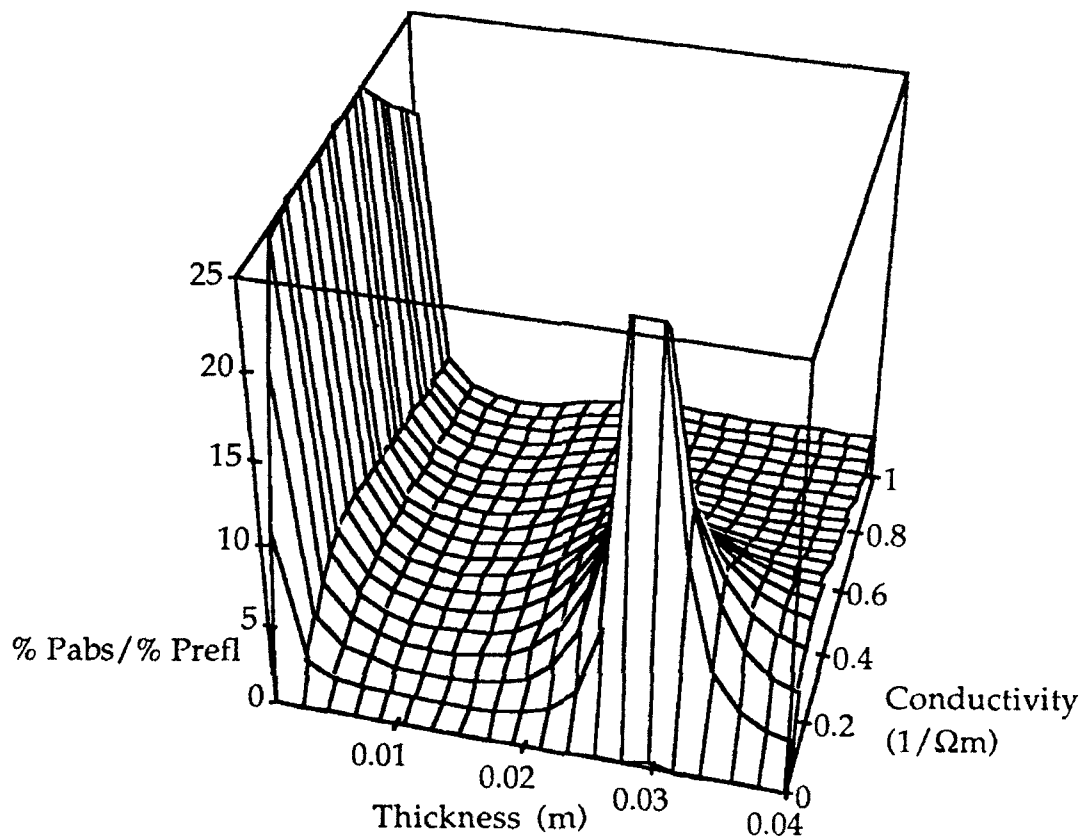


Fig. 3-15 $\%P_{\text{abs}}/\%P_{\text{refl}}$ vs thickness and conductivity

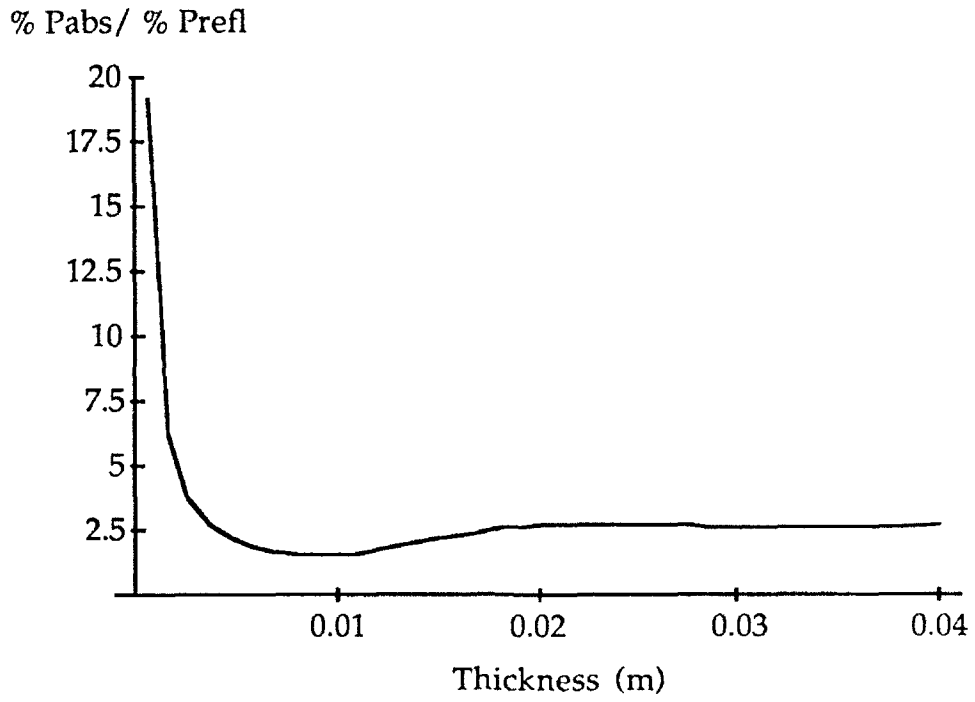


Fig. 3-16 %P_{abs}/%P_{refl} vs thickness

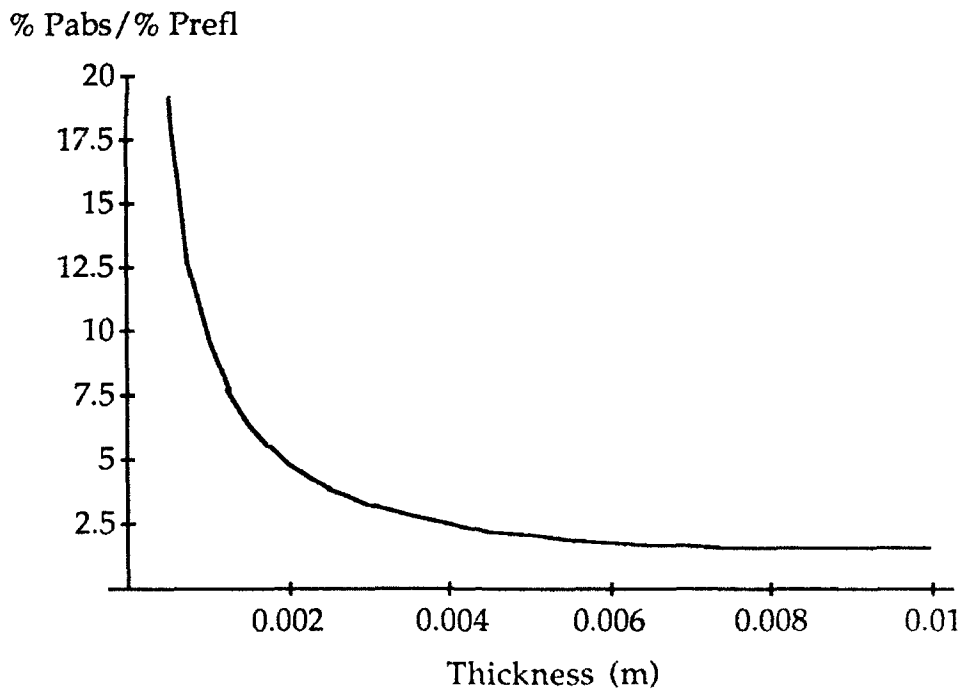


Fig. 3-17 %P_{abs}/%P_{refl} vs thickness for a thin absorber

3.5 Absorber Materials

The absorber materials chosen for fabrication were carbon- and ferrite-loaded epoxies. A liquid epoxy system is particularly useful because of its ability to be poured into molds and then machined, as well as its durability when cured. The epoxy resin chosen for this work was EPON-828 from Shell Chemicals Company. A variant of this material is EPON-815 which is a thinned version of the 828 resin. If further thinning of the resin was necessary in order to prevent excessive thickening at high loadings, Shell BGE, butyl glycidyl ether was used. In some early mixtures, a thin epoxy called Bisphenol-F was used. There are no advantages of this over a thinned version of 828 and, thus, its use was discontinued. The curing agent for all the mixes was TETA from Pacific Anchor. All of these materials can be obtained from EV Roberts & Assoc. in Culver City, CA. Cleanup can be accomplished with methyl ethyl ketone.

The carbon loadings used Ketjen EC 600 JD from Akzo Chemicals in Chicago, IL. This is a very low density, but highly conductive carbon black powder which resembles the toner in a copy machine. The ferrite loadings used Ferrite-50 from Trans-Tech, Inc. of Adamstown, MD. In contrast to the carbon, this is a very dense powder.

The difficulties in working with the two loadings are at opposite ends of the viscosity spectrum. Because the carbon has a very low density (in g/cc), mixtures containing more than about 2% (by weight) carbon in 815 epoxy are prohibitively thick. If a higher percentage of loading is desired it is necessary to thin the resin with BGE. The ferrite, however, has a very high density and is hard to keep suspended in epoxy without falling to the bottom of the mixture. Mixtures of more than 40% ferrite in 828 are very difficult to manufacture with good homogeneity. In this case, it would be necessary to start with a thicker epoxy resin. Because the emphasis of this work was on carbon-loaded epoxies, more effort was devoted to thinning to obtain good carbon loadings than thickening to obtain good ferrite loadings.

In order to prevent air bubbles from forming in the epoxy during mixing, a vacuum mixer was used. This consisted of a commercial grade food blender with a stainless steel pitcher and a reinforced rubber lid. The lid was drilled and a vacuum fitting installed. The blender was chosen because the mixing blade and the high rpm's aid in dispersing the loading agent in the resin.

3.6 Recipe for Preparation of Absorber

The epoxy resins must be used in correct proportions with the hardener. The weight ratio of TETA to 828 is 142:1000, while the ratio of

TETA to 815 is 146:1000. If it is necessary to add BGE for thinning, then extra TETA should be added in the ratio 208:1000, TETA to BGE. In all cases the percentage of carbon or ferrite loading is given as the fraction of the loading weight to the final mixture weight.

The steps taken for mixing a batch of loaded epoxy were:

- 1) Weigh out the amount of loading agent and put aside
- 2) Weigh out the amount of epoxy resin
- 3) Add thinner to the resin if necessary
- 4) Add half of the hardener to the results of 3 and mix under vacuum for 30 seconds
- 5) Add one quarter of the loading agent and mix under vacuum for 30 seconds
- 6) Repeat step 5 twice more
- 7) Add the second half of the hardener to the results of 6 and mix under vacuum for 30 seconds
- 8) Add the final quarter of the loading agent and mix under vacuum for 1 minute
- 9) Pour into a mold and let sit at room temperature for at least 5 hours
- 10) Bake the epoxy in the mold for 2 hour at 350°F.
- 11) When cool, remove the epoxy from the mold

Epoxies hardened with TETA are best hardened when the mold shape has a large surface area. For sample weights over about 50 g, the curing can become exothermic if insufficient surface area is provided. This release of heat accelerates the cure which, in turn, releases more heat with the result that within a matter of a few minutes the material will harden. This means that steps 4 to 8 must be accomplished in about 10 minutes.

Glass molds were tried, but proved unusable due to the adhesion of the hardened epoxy to the glass. Two commonly available materials which do not have adhesion problems are teflon and UHMW (Ultrahigh Molecular Weight polyethylene). Because UHMW was far less expensive than teflon it was used for the initial molding at room temperature. The hardened resin was removed from the UHMW after 5 hours and placed between teflon sheets for the high temperature bake. Both of these materials were obtained at Regal Plastics in Colorado Springs.

4 Measurement of the Electromagnetic Properties of the Absorber

One area which has been lacking in previous efforts at quantifying the thermographic mapping of electromagnetic field is that of characterizing the electric and magnetic properties of the absorbing screen at microwave frequencies. Some of the previous researchers [3,4] have used DC conductivity measurements to characterize the loss characteristics of the material. Previous attempts at measurement of the permittivity [3] have suffered from unacceptably large variations in the measured results. In order to enhance the understanding of the material parameters, a general method will be developed which permits determination of the complex permittivity and permeability at microwave frequencies using a vector network analyzer. This methodology will be used to measure well-known materials and then those fabricated as part of this work. Some of the practical considerations leading to more accurate measurements will be discussed.

The general method discussed here is that advocated by Weir [5]. This method has been shown [6] to yield accurate results when the loss tangent of the material is greater than about 0.1. The method of measurement is applicable to either waveguide or coax, but the derivation here will focus on coax. First the voltage and current in a coax will be found when a section of lossy dielectric exists between 2 lossless regions. These will then be converted to S parameters to permit comparison with measurements from a network analyzer. A conversion between S parameters and material parameters will then be developed.

4.1 Analysis of a Section of Lossy Dielectric in a Coaxial Airline

Fig. 4-1 shows a section of lossy dielectric in a coaxial airline. The incident voltage and current wave consisting of V_1^+ and I_1^+ reflects at the $z=0$ boundary giving rise to V_1^- and I_1^- ; it also transmits through the boundary giving rise to V_2^+ and I_2^+ . This plane wave reflects at the $z=d$ boundary giving rise to V_2^- and I_2^- ; it also transmits through the boundary as V_3^+ and I_3^+ . This geometry and that for plane waves given in Section 3 are very similar and, hence, lead to similar forms of solution. As in Section 3, the solution for the unknown voltages and currents will be found in the frequency domain.

The characteristic impedance and propagation constant of a section of coaxial cable are given as

$$Z = \sqrt{\frac{\mu}{\epsilon}} \frac{\ln\left(\frac{b}{a}\right)}{2\pi}$$

$$\gamma = j\omega\sqrt{\mu\epsilon} = \alpha + j\beta$$

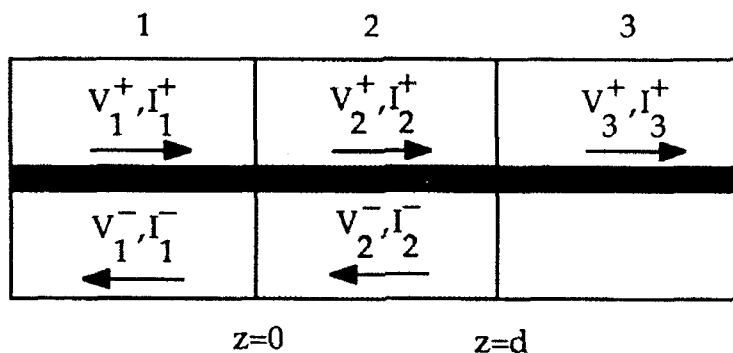


Fig. 4-1 Lossy dielectric section in a coaxial airline

In these two equations μ and ϵ are complex and represent all the losses from the dielectric section of the coax. All the effective conductivity is expressed in the term $\omega\epsilon''$. It is necessary to model all the conductivity in this manner because the network analyzer measurements will provide two complex quantities, S_{11} and S_{21} . From these only two complex quantities can be determined. If the model for the dielectric included complex μ and ϵ as well as a conductivity σ , the number of unknowns would exceed the number of measured quantities and a unique solution for the material parameters would not be possible. Wall losses have been disregarded in these forms for Z and γ .

It should be noted at this point that the ϵ'' which is measured using this method is not the same as that which was part of the electromagnetic theory in Section 2. Let us call the lossy part of the permittivity from the measurement being considered in this section ϵ''_m , the measured imaginary permittivity. The relationship between this quantity and the lossy electrical parameters of Section 2 is

$$\omega\epsilon''_m = \sigma' + \omega\epsilon''$$

Thus, the measured permittivity includes both the material's DC conductivity and the material's imaginary permittivity. However, for ease of

notation, the measured imaginary permittivity will continued to be referred to as ϵ'' .

The general forms for the voltage and current in each section of the coax are

$$\begin{aligned}
 V_1 &= V_1^+ e^{-j\beta_1 z} + V_1^- e^{+j\beta_1 z} \\
 I_1 &= \frac{1}{Z_1} \left(V_1^+ e^{-j\beta_1 z} - V_1^- e^{+j\beta_1 z} \right) \\
 V_2 &= V_2^+ e^{-\gamma_2 z} + V_2^- e^{+\gamma_2 z} \\
 I_2 &= \frac{1}{Z_2} \left(V_2^+ e^{-\gamma_2 z} - V_2^- e^{+\gamma_2 z} \right) \\
 V_3 &= V_3^+ e^{-j\beta_3(z-d)} \\
 I_3 &= \frac{1}{Z_3} V_3^+ e^{-j\beta_3(z-d)}
 \end{aligned}$$

In these forms, sections 1 and 3 are assumed to be lossless. Furthermore, it is assumed that sections 1 and 3 have air as the dielectric, thus, the characteristic impedances and propagation constants in those two regions are denoted by Z_0 and $j\beta_0$.

Continuity of the voltage and current at the boundaries of the section of dielectric yields four boundary conditions:

$$\begin{aligned}
 &\left[V_1 = V_2 \right]_{z=0} \\
 &\left[I_1 = I_2 \right]_{z=0} \\
 &\left[V_2 = V_3 \right]_{z=d} \\
 &\left[I_2 = I_3 \right]_{z=d}
 \end{aligned}$$

These four conditions are adequate to determine V_1^- , V_2^+ , V_2^- and V_3^+ in

terms of V_1^+ :

$$V_1^- = V_1^+ \frac{\Gamma(1-P^2)}{1-\Gamma^2 P^2}$$

$$V_2^+ = V_1^+ \frac{\Gamma+1}{1-\Gamma^2 P^2}$$

$$V_2^- = V_1^+ \frac{-\Gamma P^2(\Gamma+1)}{1-\Gamma^2 P^2}$$

$$V_3^+ = V_1^+ \frac{P(1-\Gamma^2)}{1-\Gamma^2 P^2}$$

where:

$$\Gamma = \frac{Z_2 - Z_0}{Z_2 + Z_0}$$

$$P = e^{-\gamma_2 d}$$

Assuming that the left side of the coax in Fig. 4-1 is connected to port 1 of a network analyzer and the right side to port 2, the measured S parameters are related to the voltages as

$$S_{11} = \frac{V_1^-}{V_1^+} = \frac{\Gamma(1-P^2)}{1-\Gamma^2 P^2} \quad (4-1)$$

$$S_{21} = \frac{V_3^+}{V_1^+} = \frac{P(1-\Gamma^2)}{1-\Gamma^2 P^2} \quad (4-2)$$

4.2 Relating Material Parameters to Measured S-Parameters

Equations 4-1 and 4-2 give the measured S parameters in terms of the reflection coefficient Γ and propagation term P . A very tedious inversion of these two equations yields

$$\Gamma = \chi \pm \sqrt{\chi^2 - 1} \quad (4-3)$$

$$P = \frac{S_{11} + S_{21} - \Gamma}{1 - (S_{11} + S_{21})\Gamma} \quad (4-4)$$

where

$$\chi = \frac{S_{11}^2 - S_{21}^2 + 1}{2S_{11}} \quad (4-5)$$

Because of the symmetry in equations 4-1 and 4-2, the inversion can also yield

$$P = v \pm \sqrt{v^2 - 1}$$

$$\Gamma = \frac{S_{11} + S_{21} - P}{1 - (S_{11} + S_{21})P}$$

where

$$v = \frac{S_{21}^2 - S_{11}^2 + 1}{2S_{21}}$$

The form in equations 4-3 to 4-5 will be used for the remainder of this work.

From the definitions of Γ and P , the material parameters can be found as functions of Γ and P .

$$\sqrt{\frac{\mu_{r2}}{\epsilon_{r2}}} = \frac{1 + \Gamma}{1 - \Gamma} = x \quad (4-6)$$

$$\sqrt{\mu_{r2}\epsilon_{r2}} = \frac{-j}{\omega d \sqrt{\mu_0 \epsilon_0}} \ln\left(\frac{1}{P}\right) = y \quad (4-7)$$

The material parameters can thus be found as

$$\mu_{r2} = xy \quad (4-8)$$

$$\epsilon_{r2} = \frac{y}{x} \quad (4-9)$$

4.3 Data Processing for the Determination of Material Parameters

Determining the complex-valued material parameters from the measured S parameters can be accomplished by application of equations 4-1 to 4-9. The computer code used to perform the data reduction is given in Appendix B. There are, however, two issues which need to be addressed before this data reduction can occur. These are the subjects of the next two sections.

4.3.1 Resolving Multiple Solutions by Velocity Considerations

Equation 4-7 has a multiplicity of solutions due to the complex natural

logarithm. Expanding this equation yields

$$y = \frac{-j}{\omega d \sqrt{\mu_0 \epsilon_0}} \ln \left(e^{\alpha d} e^{j\beta d} \right) = \frac{-j}{\omega d \sqrt{\mu_0 \epsilon_0}} (\alpha d + j(\beta d + 2\pi n))$$

where n is an integer. The multiple values of n each lead to different combinations of μ and ϵ which could yield the measured S parameters. That is, the mapping of S parameters to μ and ϵ is not 1-to-1. In order to resolve this ambiguity, some other quantity must determine which value of n is correct. A quantity which can be derived from the measured data is the group delay of the signal. Because each combination of μ and ϵ leads to different predicted group delays through the sample, a comparison of the measured and predicted group delays will determine the correct value of n .

The group delay can be determined from the measured data as

$$\tau_g = -\frac{\partial}{\partial \omega} \langle P \rangle$$

where $\langle P \rangle$ is the radian phase angle of the term P in equation 4-4. Once a value of n is chosen, the complex material parameters for that choice of n , μ_n and ϵ_n , can be calculated. The group delay can then be calculated for this choice of n as

$$\tau_{gn} = \frac{d}{\sqrt{2}} \sqrt{\mu'_n \epsilon'_n - \mu''_n \epsilon''_n + \sqrt{(\mu'_n \epsilon'_n - \mu''_n \epsilon''_n)^2 - (\mu''_n \epsilon'_n + \mu'_n \epsilon''_n)^2}}$$

where

$$\begin{aligned} \mu_n &= \mu'_n - j\mu''_n \\ \epsilon_n &= \epsilon'_n - j\epsilon''_n \end{aligned}$$

By comparing the experimentally determined group delay, τ_g , and the group delay for a particular choice of n , τ_{gn} , the correct value of n can be determined. This correct value of n then yields the correct values of μ and ϵ . Occasionally, due to noise in the data, an incorrect choice of μ and ϵ is chosen, as can be seen, for example, in the spikes in Fig. 4-17.

4.3.2 Network Analyzer Reference Plane Adjustment

Another modification to the measured data involves moving the reference plane of the network analyzer to each side of the sample. Most network analyzers have this feature built-in. However, for this work a manual adjustment was made to the reference planes. Fig. 4-2 illustrates the movement of the reference planes.

The network analyzer makes measurements of S_{11}' and S_{21}' at the points at which it was calibrated. However, equations 4-1 through 4-5 use the

values just at the ends of the sample; these are denoted by S_{11} and S_{21} . The conversion from the measured values to those which would have been measured at the ends of the sample are

$$S_{11} = S_{11}' e^{j\beta_0 2a}$$

$$S_{21} = S_{21}' e^{j\beta_0(a+b)}$$

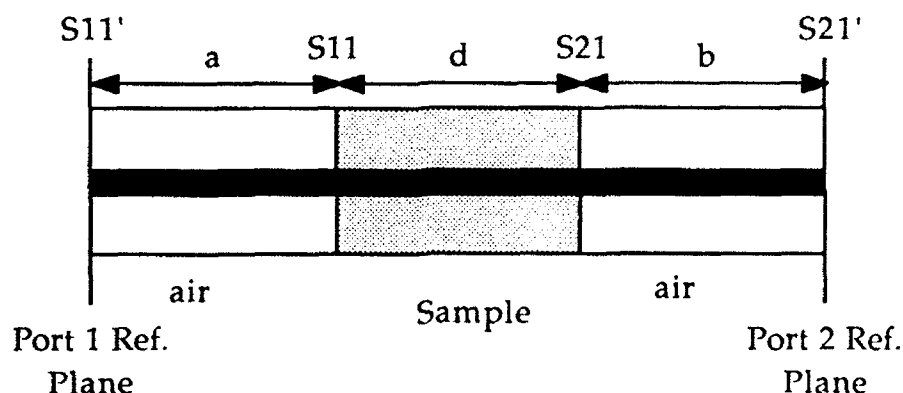


Fig. 4-2 Network analyzer reference plane movement

where

$$\beta_0 = \omega \sqrt{\mu_0 \epsilon_0}$$

It should be noted that these reference plane extensions do not take into account losses in the coax, however, for a good quality coax these losses are small.

4.4 Measurement Equipment and Procedures

Some of the early measurements were made on an HP 8510A network analyzer, while the rest were made on a HP 8720A. A full two port calibration was performed prior to each measurement session. The reference planes after this calibration were the ends of the cables on the ports of the analyzer. A fairly slow sweep rate of 10 seconds was used along with 4 trace averaging. The data was captured over GPIB and processed using the code in Appendix B.

Two very important quantities are the reference plane offsets a and b in Fig. 4-2. It is extremely important that the position of the sample in the coax be known to at least ten degrees of phase or less. As an example, a 1 mm uncertainty in the position of the sample at 6 GHz is 7.2 degrees of phase, but at 10 GHz it is 12 degrees. This is critical because the complex material parameters are determined from complex S parameters. A variation in phase

of the S parameters can cause large variations in the material parameters. This partly explains the instability in the data at higher frequencies. Most measurements with the network analyzer involve magnitude only data. The need for accurate phase data makes the measurement more difficult. A jig to precisely position the sample in the coax is quite helpful at reducing the uncertainty in the sample's position. The measurements showed good repeatability when the alignment jig was used.

Because the measurement is being made at the end of two to three foot long teflon dielectric cables, a short and low loss sample may not cause a significant change in the S parameters. Longer samples have more effect on the S parameters and, thus, provide better data. The same is true of higher loss samples. Hewlett Packard believes that this method is accurate if the loss tangent is greater than about 0.1 [6]. Although no attempt was made to verify this claim, the results do seem better for the higher loss samples.

One final note about the measurements is in order. Due to the uncertainty in the S_{11} measurement, the data will typically yield bad values when the sample is a multiple of a quarter of a wavelength. (This is a quarter of a wavelength in the sample material, not free space.) The remedy for this is to make the sample short enough that the first quarter-wavelength frequency is above the measurement band. Notice that this is in opposition to the desire for a long sample size stated above. In order to resolve these opposing constraints, the sample length for the loaded epoxies was chosen to be as long as possible while still staying just below the frequency of the first discontinuity. This was not done for the air or nylon samples and, therefore, plots for these materials display the discontinuities.

4.5 Material Measurement Results

Figs. 4-3 and 4-4 show the complex material parameters for an air filled 10 cm coax. The data are within 2% of the expected values except at the quarter wavelength frequencies. The imaginary parts should be zero, but are not. This could be due to experimental uncertainty or to incorporation of wall losses as dielectric losses, since the theory does not account for wall losses. As is normally the case for this method, the lower frequencies are more accurate than the higher frequencies.

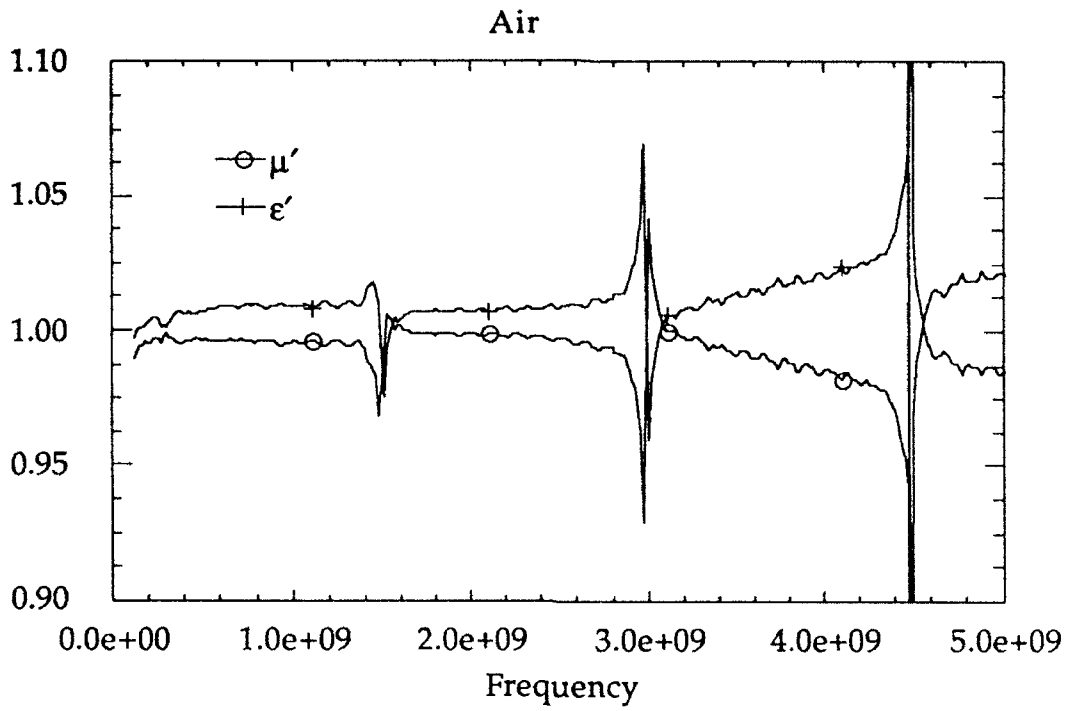


Fig. 4-3 Real permittivity and permeability of air

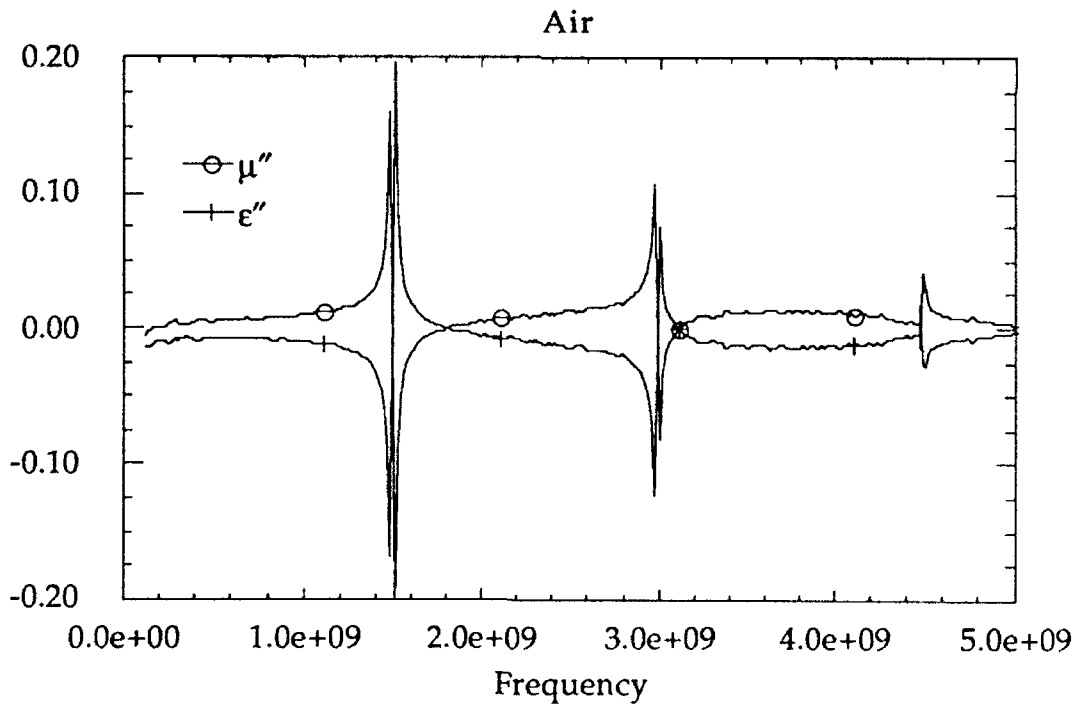


Fig. 4-4 Imaginary permittivity and permeability of air

4.5.1 Comparison with Other Measurements

Figs. 4-5 and 4-6 show the real and imaginary parts of the relative permittivity and permeability for teflon. Von Hippel [7] gives the value of $\epsilon_r = 2.1 - j3.15 \times 10^{-4}$ at 3 GHz. Because teflon is essentially non-magnetic, $\mu_r \sim 1$. As discussed above, the measurement of the imaginary parts of permittivity and permeability are not accurate due to the low-loss nature of the material. However, the real parts are in good agreement with the previously published values.

Figs. 4-7 and 4-8 show the real and imaginary parts of the relative permittivity and permeability for nylon. Von Hippel gives the value of $\epsilon_r = 3.03 - j4.22 \times 10^{-3}$ at 3 GHz. As with teflon, nylon is essentially non-magnetic, thus, $\mu_r \sim 1$.

4.5.2 Results for Loaded Epoxies

Each of the plots in this section show the variation of the real and imaginary permittivity and permeability with frequency. In addition, an effective conductivity $\sigma = -\omega \epsilon_0 \epsilon''$ has been plotted with the imaginary parts.

Figs. 4-9 and 4-10 show the measured material parameters for a 20% ferrite loading. The recipe for this mixture is shown in Table 4-1.

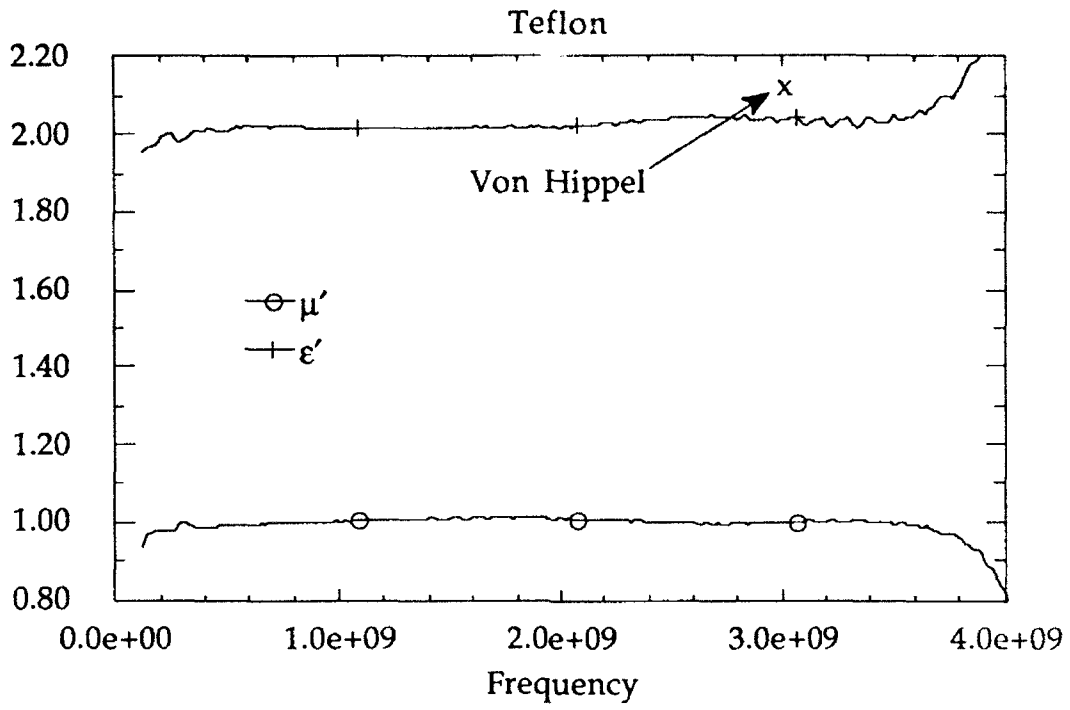


Fig. 4-5 Real permittivity and permeability of teflon

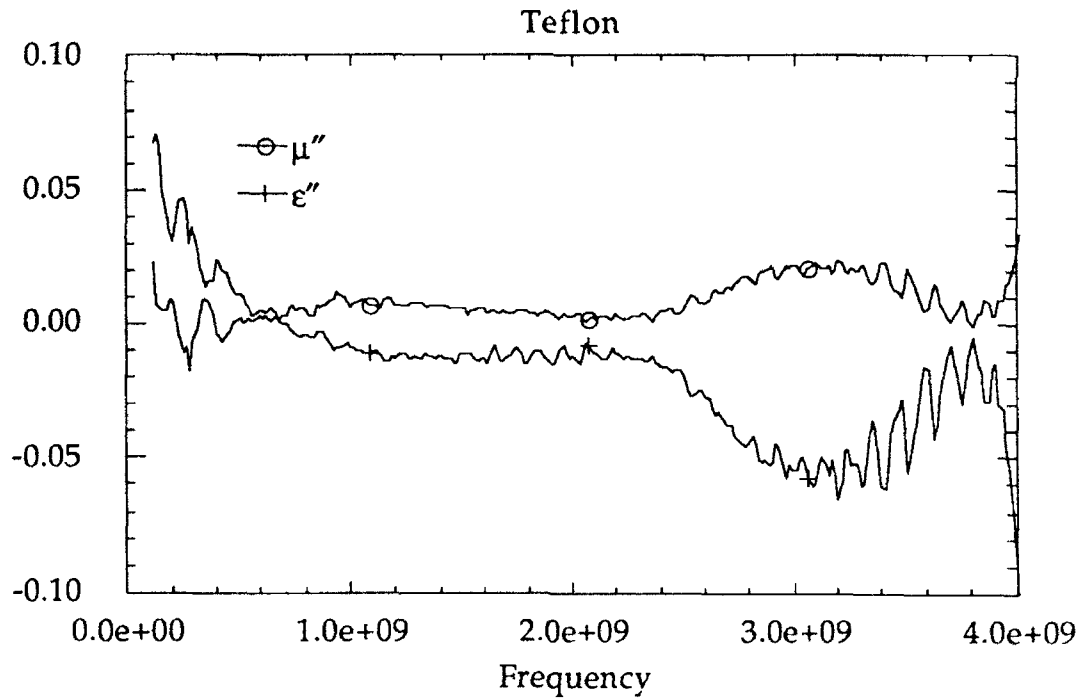


Fig. 4-6 Imaginary permittivity and permeability of teflon

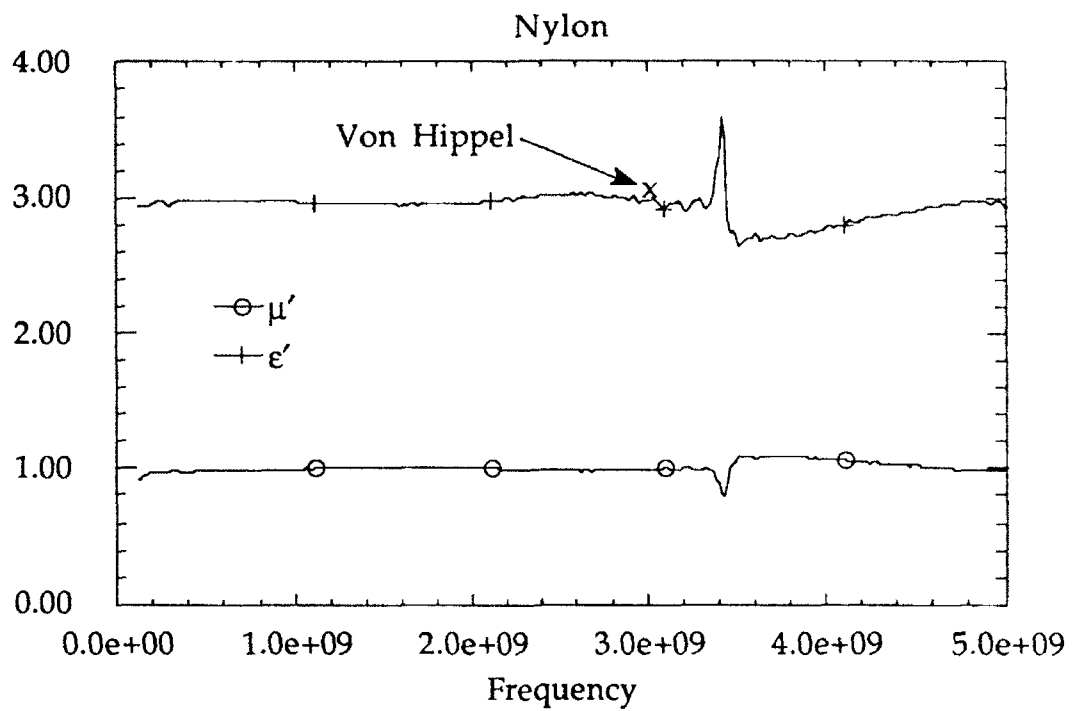


Fig. 4-7 Real permittivity and permeability of nylon

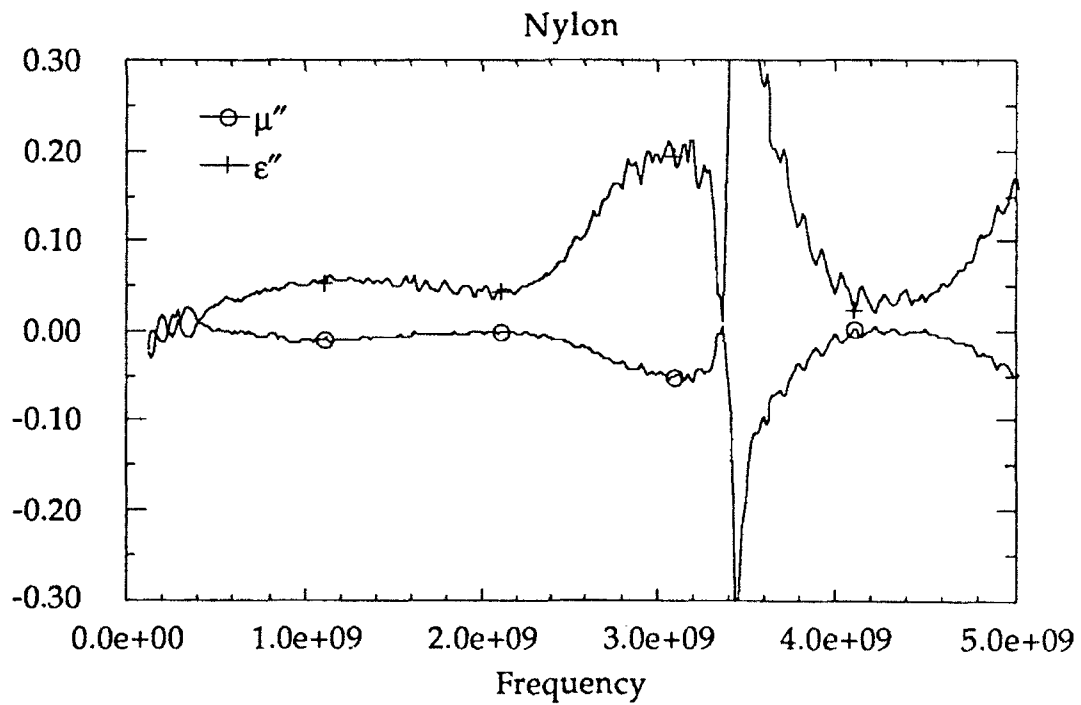


Fig. 4-8 Imaginary permittivity and permeability of nylon

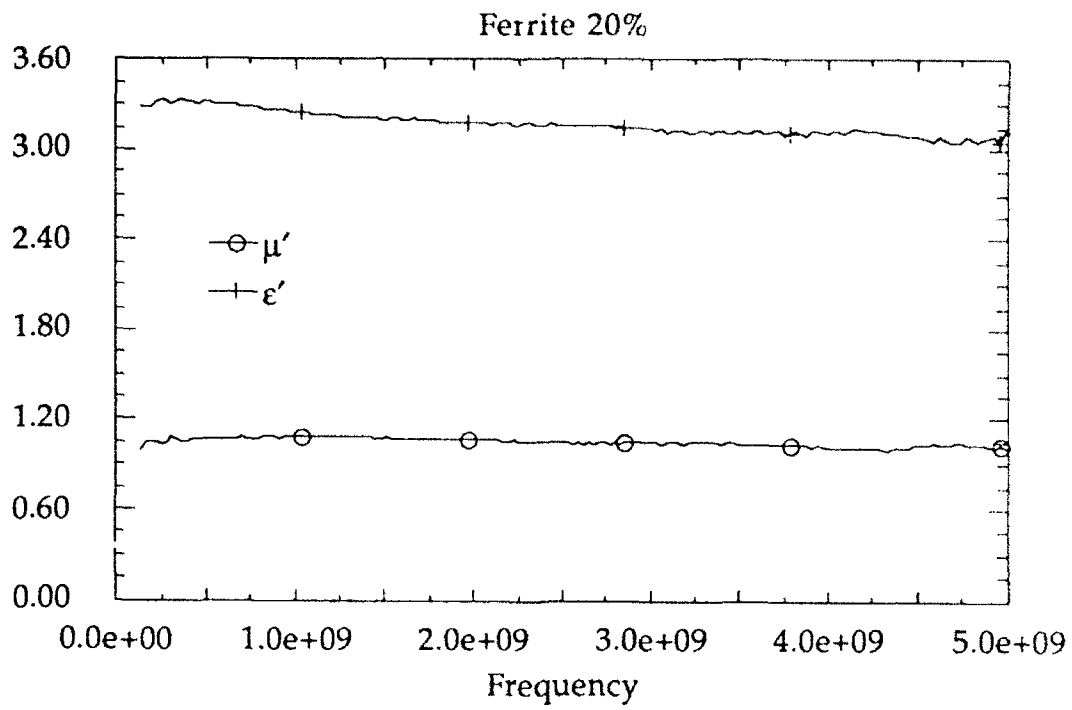


Fig. 4-9 Real permittivity and permeability of 20% ferrite loaded epoxy

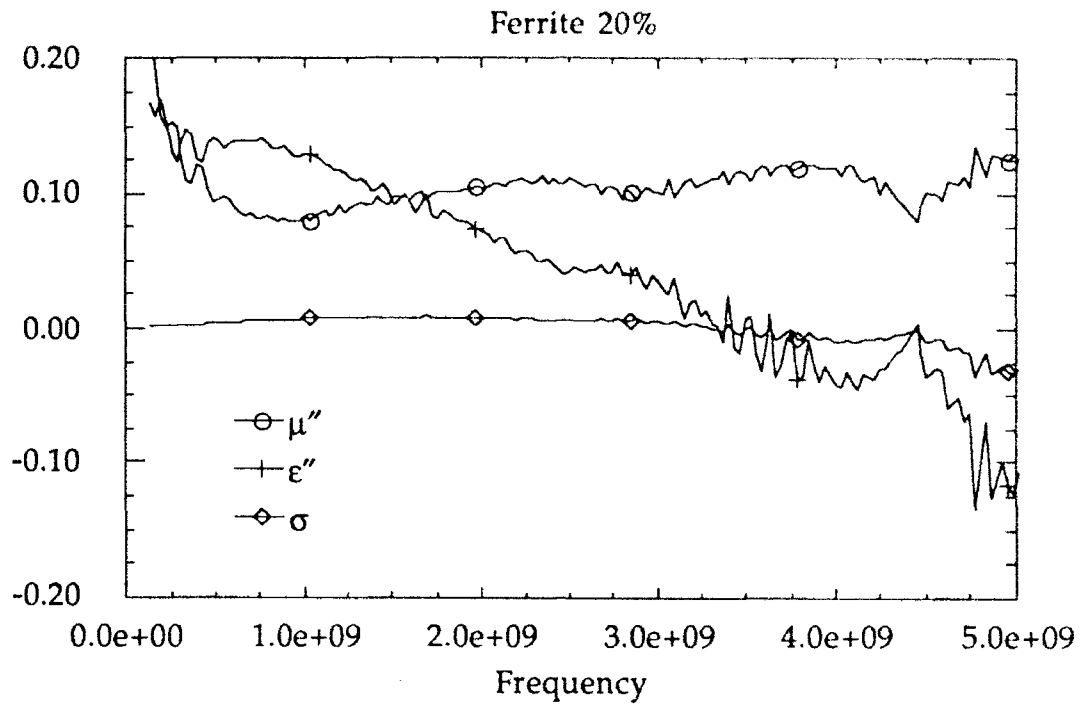


Fig. 4-10 Imaginary permittivity, permeability and effective conductivity of 20% ferrite loaded epoxy

Table 4-1 20% ferrite recipe

Additive	grams
EPON-828	50
Bisphenol-F	20
Ferrite-50	20.09
TETA	10.38

Figs. 4-11 and 4-12 show the measured material parameters for a 30% ferrite loading. The recipe for this mixture is shown in Table 4-2.

Table 4-2 30% ferrite recipe

Additive	grams
EPON-828	100
Ferrite-50	48.9
TETA	14.2

Figs. 4-13 and 4-14 show the measured material parameters for a 40% ferrite loading. The recipe for this mixture is shown in Table 4-3.

Table 4-3 40% ferrite recipe

Additive	grams
EPON-828	200
Ferrite-50	97.9
TETA	28.4

Figs. 4-15 and 4-16 show the measured material parameters for a 1.7% carbon loading. The recipe for this mixture is shown in Table 4-4.

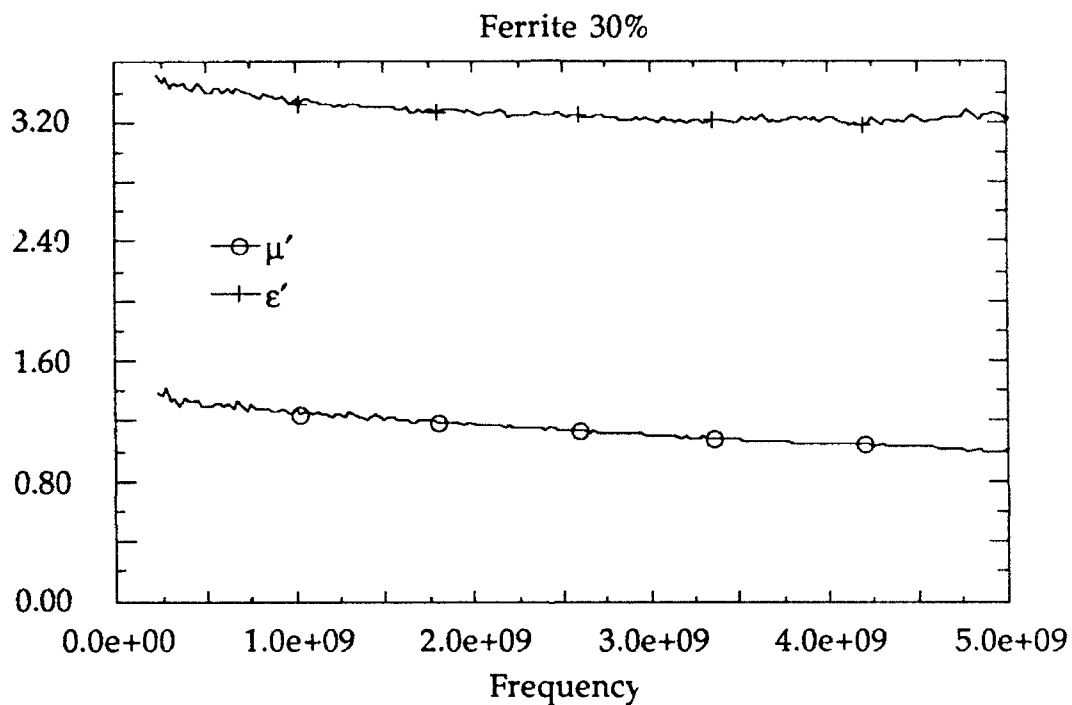


Fig. 4-11 Real permittivity and permeability of 30% ferrite loaded epoxy

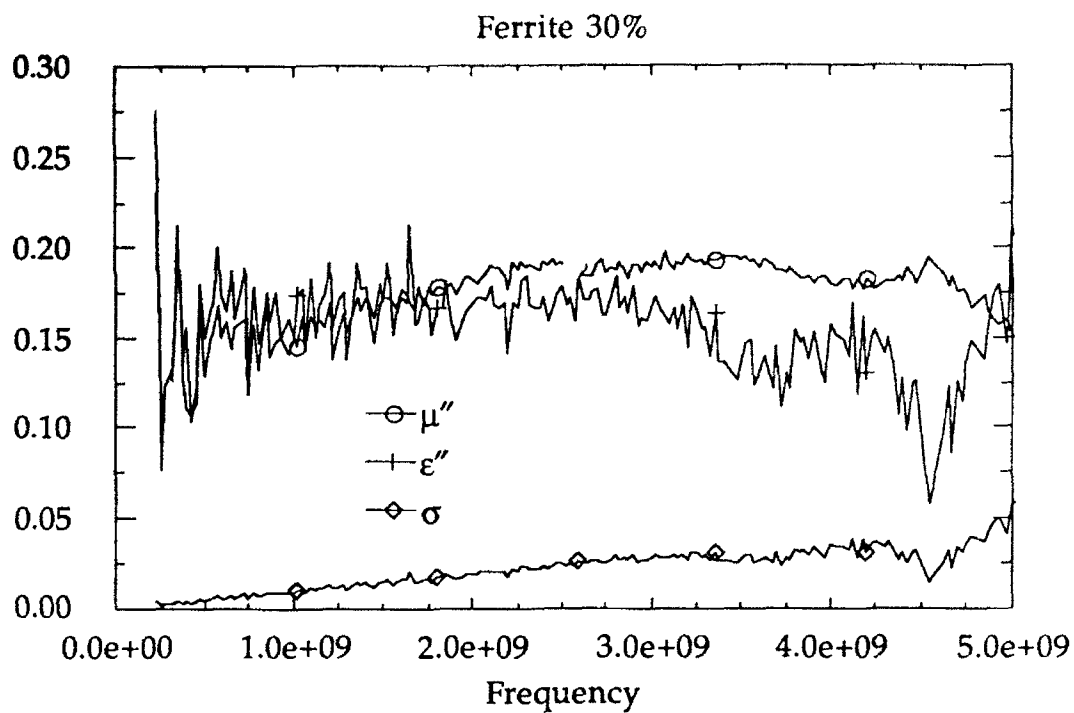


Fig. 4-12 Imaginary permittivity, permeability and effective conductivity of 30% ferrite loaded epoxy

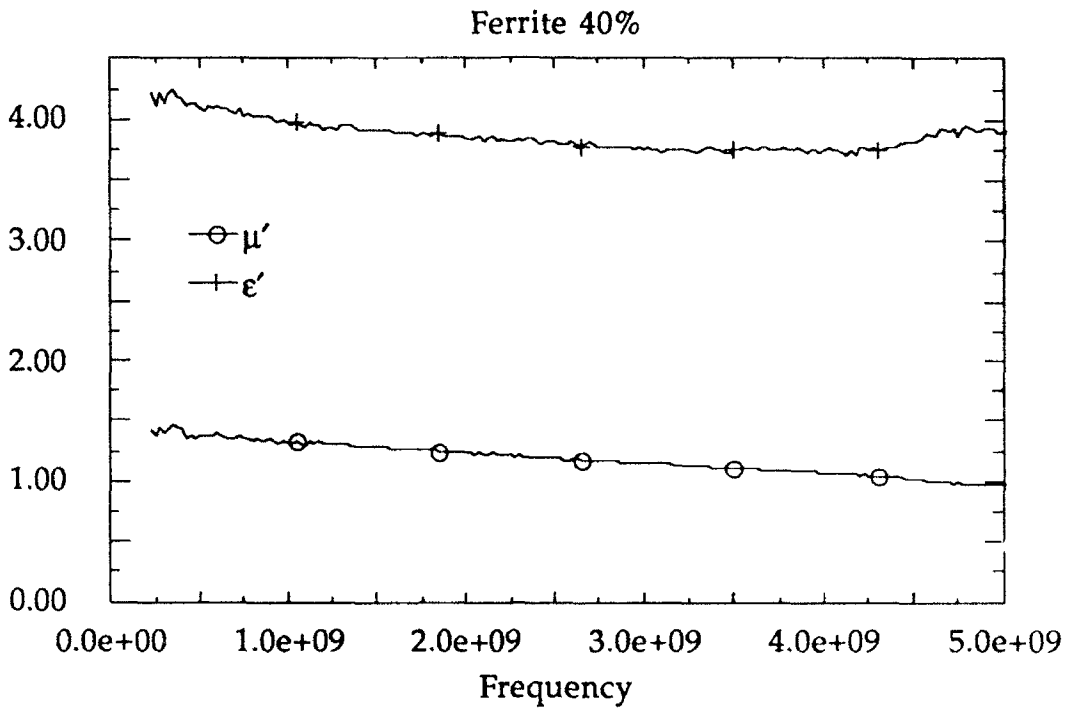


Fig. 4-13 Real permittivity and permeability of 40% ferrite loaded epoxy

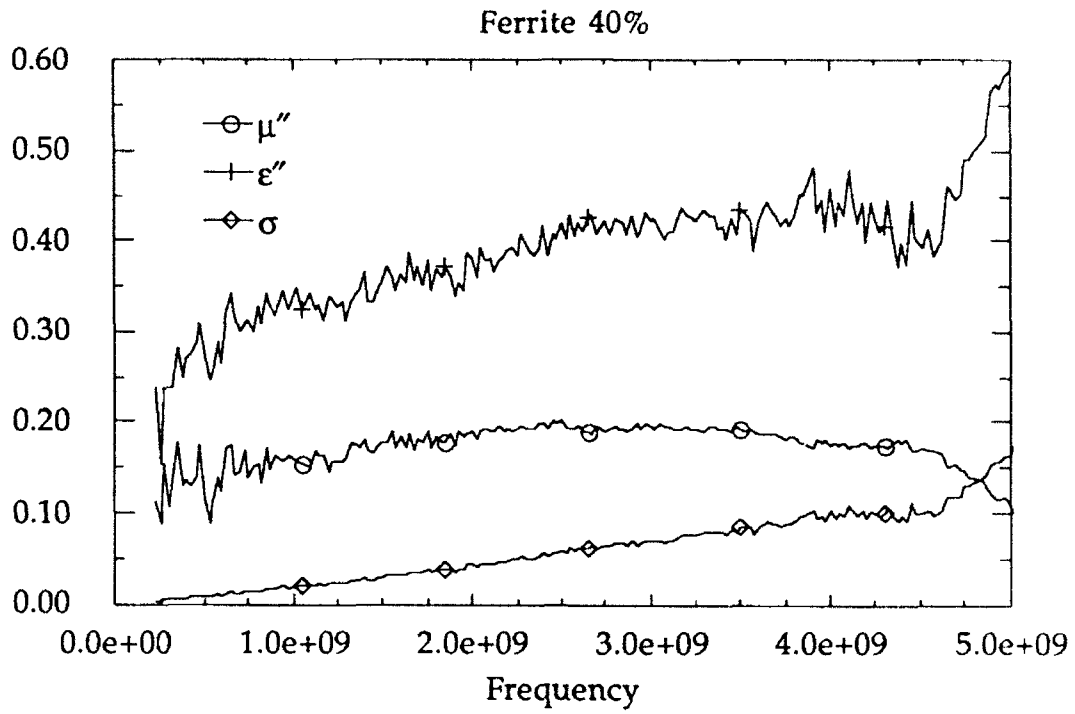


Fig. 4-14 Imaginary permittivity, permeability and effective conductivity of 40% ferrite loaded epoxy

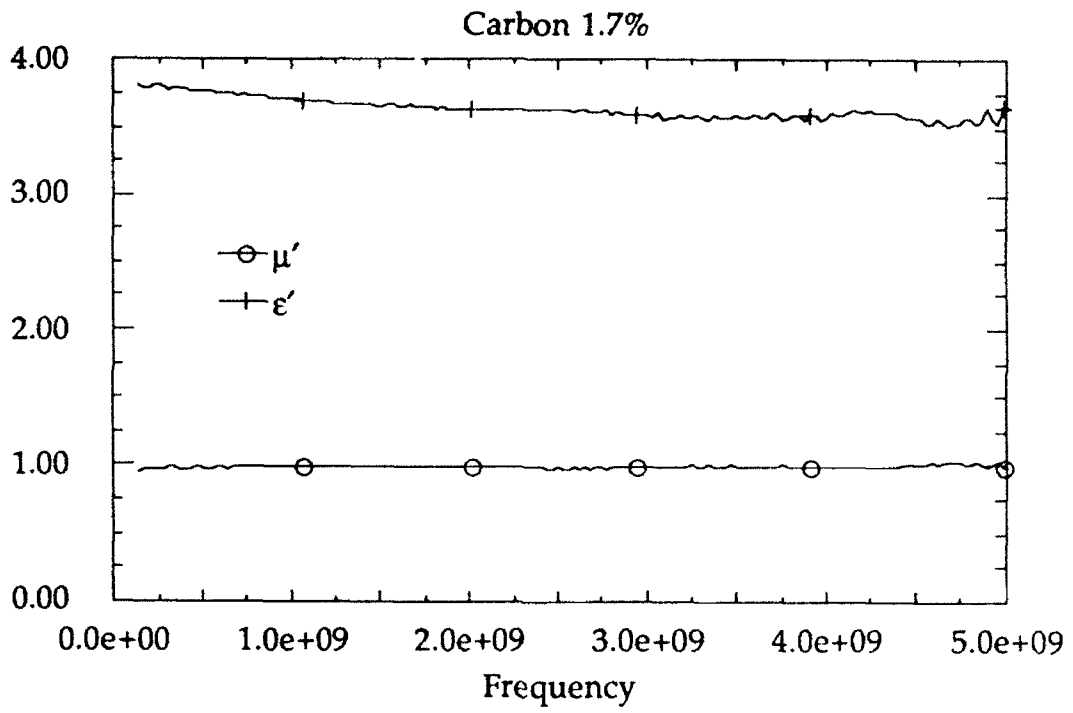


Fig. 4-15 Real permittivity and permeability of 1.7% carbon loaded epoxy

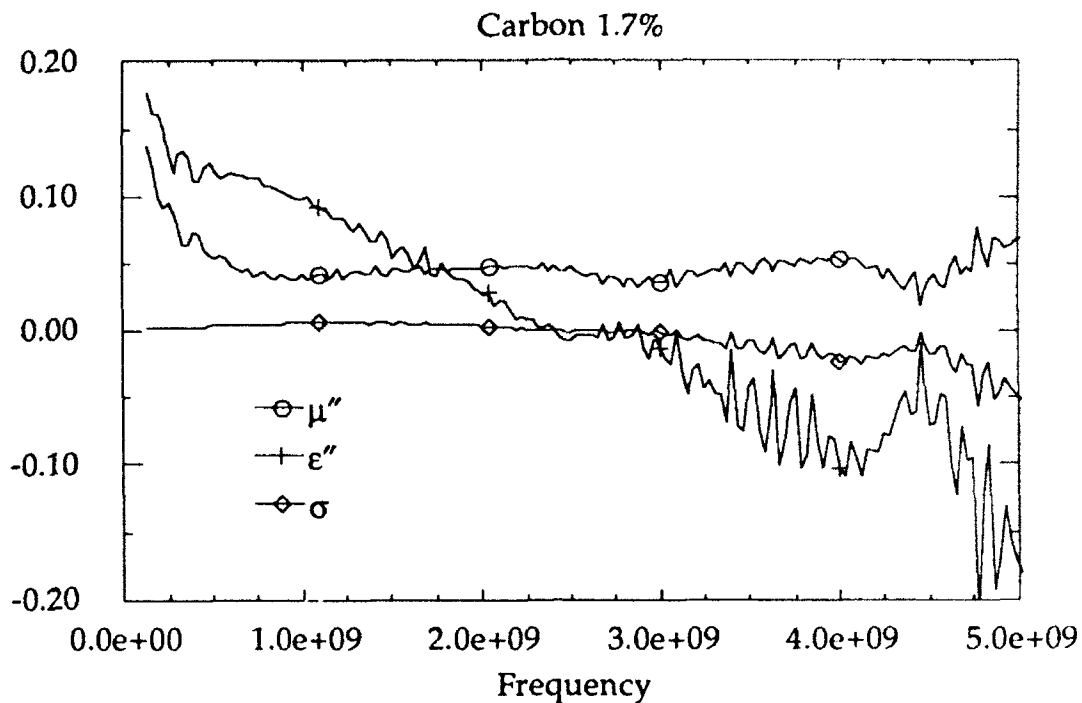


Fig. 4-16 Imaginary permittivity, permeability and effective conductivity of 1.7% carbon loaded epoxy

Table 4-4 1.7% carbon recipe

Additive	grams
EPON-828	24.125
Bisphenol-F	20.76
EC 600 JD	0.875
TETA	5.71

Figs. 4-17 and 4-18 show the measured material parameters for a 4% carbon loading. The recipe for this mixture is shown in Table 4-5.

Table 4-5 4% carbon recipe

Additive	grams
EPON-815	150
BGE	6
EC 600 JD	7.5
TETA	23.6

The desired parameters for the absorbing screen were $\sigma=1$ ($\omega\epsilon''=6$), $\epsilon'=3$ and $\mu'=1$ at 3 GHz. The 4% carbon results come close on all but the ϵ' . This is

due to the carbon increasing both the real and imaginary parts of ϵ .

Figs. 4-15 and 4-16 show the measured material parameters for a 2.3% carbon and 22.5% ferrite loading. The recipe for this mixture is shown in Table 4-6. This mixture ratio gives the percentage of loadings disregarding the weight from the other loading component.

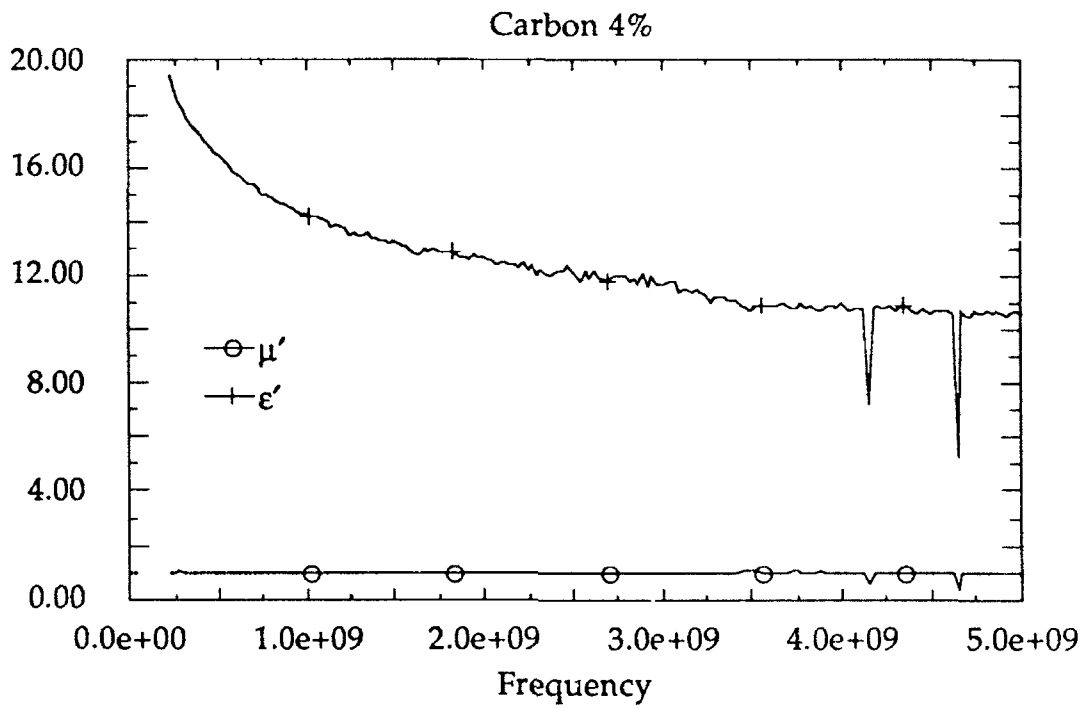


Fig. 4-17 Real permittivity and permeability of 4% carbon loaded epoxy

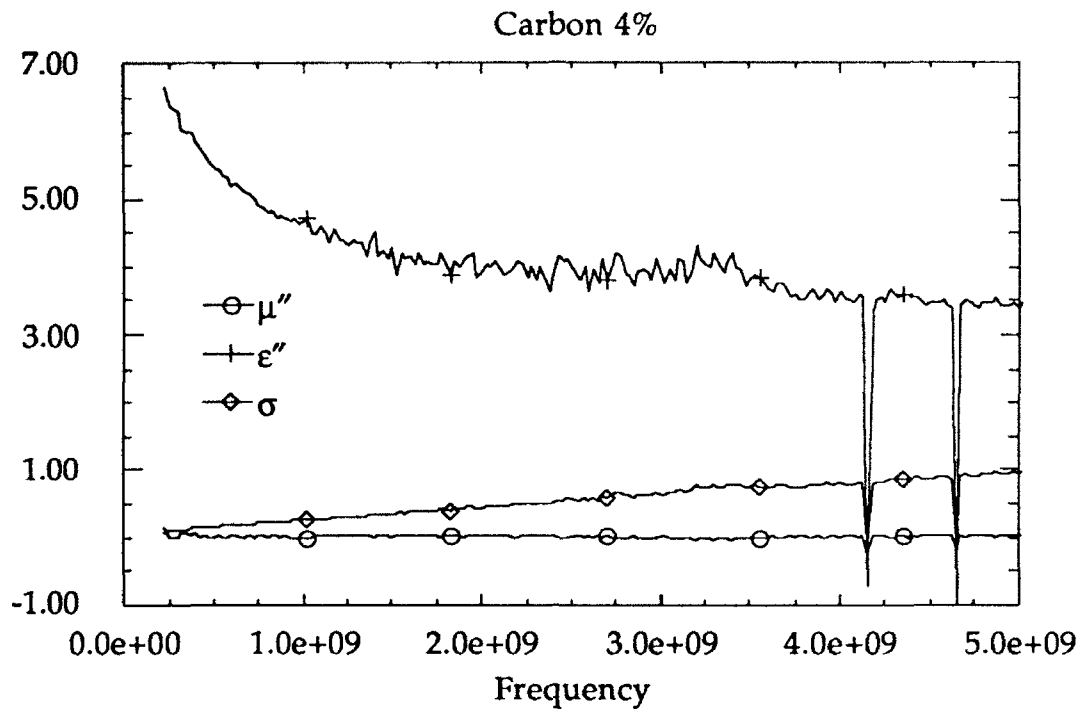


Fig. 4-18 Imaginary permittivity, permeability and effective conductivity of 4% carbon loaded epoxy

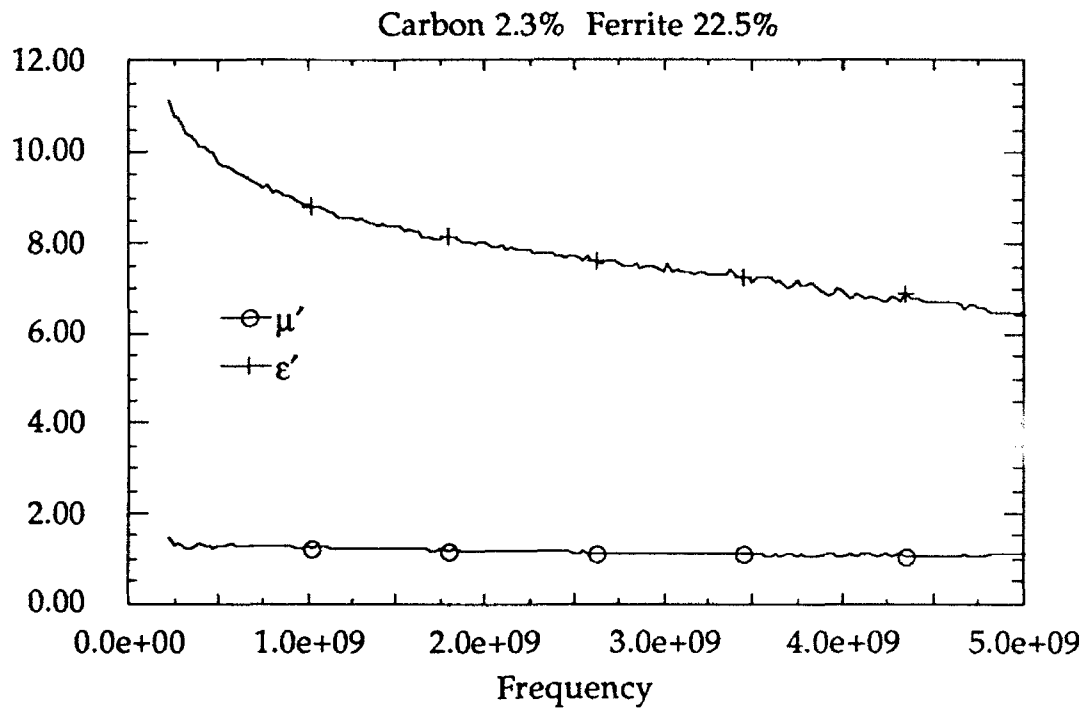


Fig. 4-19 Real permittivity and permeability of 2.3% carbon-
22.5% ferrite loaded epoxy

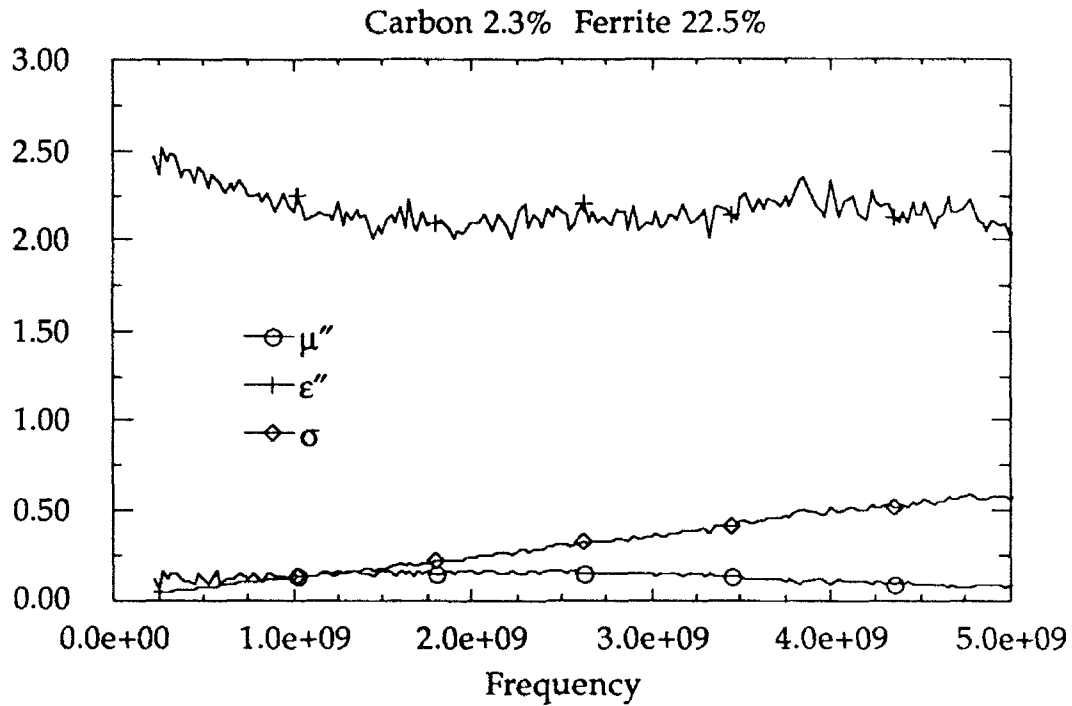


Fig. 4-20 Imaginary permittivity, permeability and effective conductivity of 2.3% carbon-22.5% ferrite loaded epoxy

Table 4-6 2.3% carbon-22.5% ferrite recipe

Additive	grams
EPON-815	150
EC 600 JD	4
Ferrite-50	50
TETA	21.9

Table 4-7 contains a summary list of material parameters at selected frequencies for the samples above.

Table 4-7 Material parameters for prepared samples

Sample	Frequency (GHz)	μ_r	ϵ_r
20% ferrite	3.0	1.047-j.1003	3.125-j.0291
30% ferrite	3.0	1.107-j.1890	3.212-j.1680
40% ferrite	3.0	1.152-j.1956	3.741-j.4223
1.7% carbon	1.0	.9886-j.0430	3.707-j.0980
4% carbon	3.025	.9780-j.0067	11.68-j3.755
2.3% carbon- 22.5% ferrite	3.0	1.115-j.1425	7.376-j2.085

4.6 DC Conductivity Measurements

The measurement of conductivity using a standard method is illustrated in Fig. 4-21. The total resistance of the block of material is given as

$$R = \frac{L}{\sigma wh}$$

The conductivity is, thus, given as

$$\sigma = \frac{L}{Rwh}$$

The carbon 4% sample measurement had a DC conductivity of 0.066 (1/Ωm). Fig. 4-22 shows the extrapolation of the high frequency measurement of the effective conductivity ($-\omega\epsilon_0\epsilon''$) down to a DC value by means of a straight line.

This predicts a DC conductivity of about 0.05 1/Ωm, in good agreement with the measured value. Recall that the measured imaginary permittivity includes both the material's DC conductivity and the material's imaginary permittivity, as explained in Section 4.1. Thus, the extrapolation of the measured imaginary permittivity down to DC should yield a value close to the measured DC conductivity, as is the case in Fig. 4-22.

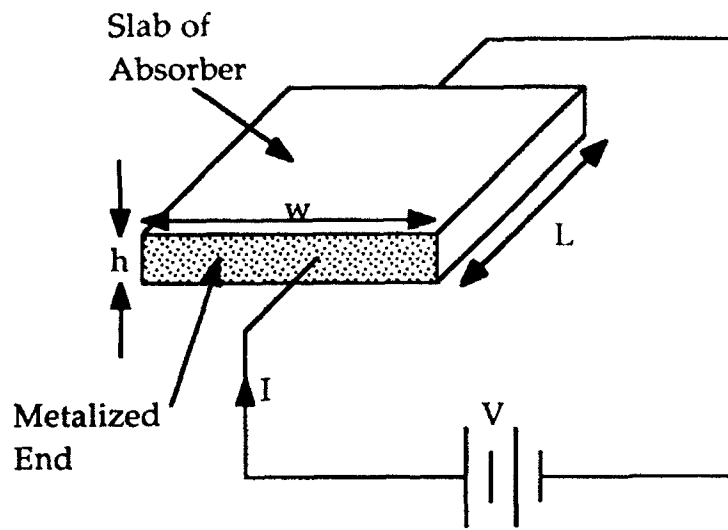


Fig. 4-21 DC Measurement of Conductivity

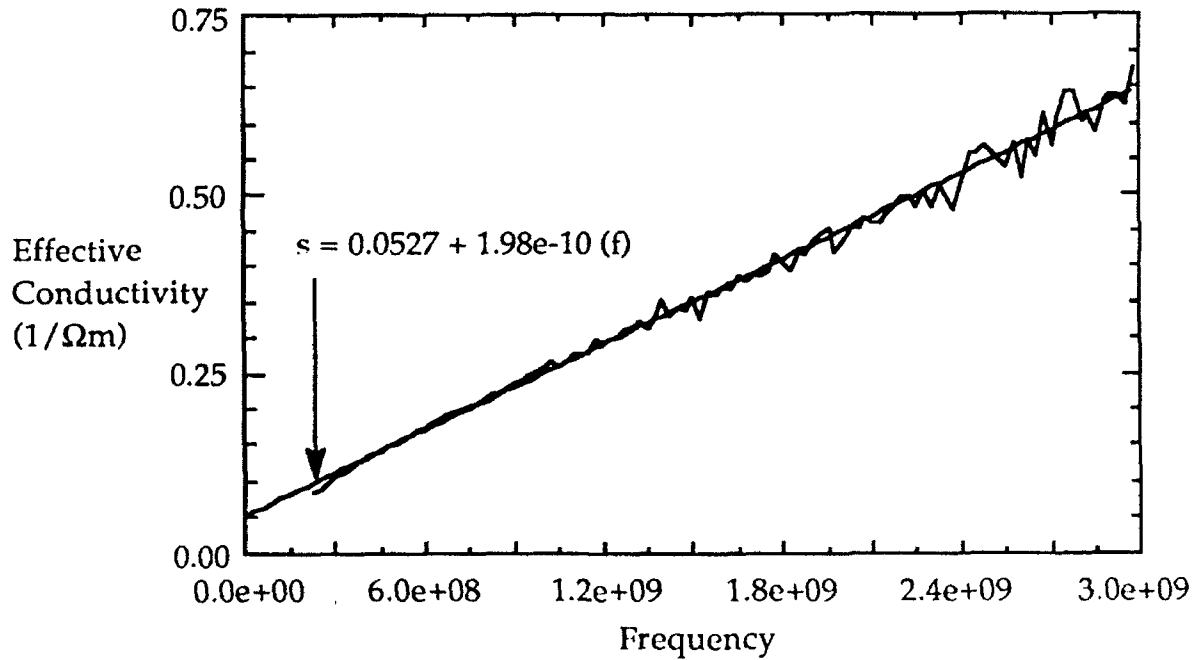


Fig. 4-22 Extrapolated effective conductivity for 4% carbon loaded epoxy

References

- 1) K Iizuka, Engineering Optics, Second Edition, Springer-Verlag, 1987.
- 2) RWP King, The Theory of Linear Antennas, Harvard University Press, 1956.
- 3) VM Martin, "Microwave Interaction with Thin Multiple Conductive Coatings", PhD Thesis, Univ. of Colo., Colo. Spgs., 1982.
- 4) GD Wetlaufer, "Optimization of Thin-Screen Material Used in Infrared Detection of Microwave Induced Surface Currents at 2-3 GHz", MSEE Thesis, Univ. of Colo., Colo. Spgs., 1985.
- 5) WB Weir, "Automatic Measurement of Complex Dielectric Constant and Permeability at Microwave Frequencies", Proceedings of the IEEE, Volume 62, Number 1, January 1974.
- 6) Measuring Dielectric Constant with the HP 8510 Network Analyzer, HP Product note 8510-3, Hewlett Packard, August 1985.
- 7) AR Von Hippel, ed., Dielectric Materials and Applications, John Wiley & Sons, 1954.

Appendix A Mathematica Equations for Electromagnetic Analyses

This section lists the the equations used in Mathematica for the generation of the plots in Section 3.

A.1 Absorber Equations

The following input can be used to calculate the power flow in and around a semi-infinite slab of absorber.

```
eps0=8.854*10^-12;  
mu0=4*Pi*10^-7;  
etaair=N[Sqrt[mu0/eps0]];  
  
pinside[freq_,epsrdiel_,d_,sigma_]:=  
  Block[  
    {omega,gammadiel,alpha,beta,etadiel,p,gamma,  
     erefl,powerpersqm},  
  
    omega=N[2*Pi*freq];
```

```

gammadiel=N[I*omega*Sqrt[mu0*eps0*epsrdiel]*
  Sqrt[1+sigma/(I*omega*eps0*epsrdiel)]];
alpha=Re[gammadiel];
beta=Im[gammadiel];
etadiel=
  N[Sqrt[mu0/(eps0*epsrdiel+sigma/(I*omega))]];
p=N[E^(-gammadiel*d)];
gamma=N[(etadiel-etaair)/(etadiel+etaair)];

erefl=N[gamma*(1-p^2)/(1-(gamma^2)(p^2))];

powerpersqm=1/(2*etaair)*
  (1-Abs[erefl]^2+2*I*Im[erefl]);

Return[N[powerpersqm]];
];

```

```

pabs[freq_epsrdiel_d_sigma_]:=
Block[
  {omega,gammadiel,alpha,beta,etadiel,p,gamma,
  e2plus,e2minus,powerpersqm},

  omega=N[2*Pi*freq];
  gammadiel=N[I*omega*Sqrt[mu0*eps0*epsrdiel]*
    Sqrt[1+sigma/(I*omega*eps0*epsrdiel)]];
  alpha=Re[gammadiel];
  beta=Im[gammadiel];
  etadiel=
    N[Sqrt[mu0/(eps0*epsrdiel+sigma/(I*omega))]];
  p=N[E^(-gammadiel*d)];
  gamma=N[(etadiel-etaair)/(etadiel+etaair)];

  e2plus=N[(gamma+1)/(1-(gamma^2)(p^2))];
  e2minus=N[(-gamma*p^2)*(gamma+1)/
    (1-(gamma^2)(p^2))];

  powerpersqm=sigma/4*
    ((Abs[e2minus]^2)/alpha*(E^(2*alpha*d)-1)-
    (Abs[e2plus]^2)/alpha*(E^(-2*alpha*d)-1)+
    (2/beta)*Re[e2plus*Conjugate[e2minus]*
    I*(E^(-2*I*beta*d)-1)]);

  Return[N[powerpersqm]];
];

```

```

ptrans[freq_epsrdiel_d_sigma_]:=

```

```

Block[
  {omega,gammadiel,alpha,beta,etadiel,p,gamma,
  etrans,powerpersqm},

  omega=N[2*Pi*freq];
  gammadiel=N[I*omega*Sqrt[mu0*eps0*epsrdiel]*
    Sqrt[1+sigma/(I*omega*eps0*epsrdiel)]];
  alpha=Re[gammadiel];
  beta=Im[gammadiel];
  etadiel=
    N[Sqrt[mu0/(eps0*epsrdiel+sigma/(I*omega))]];
  p=N[E^(-gammadiel*d)];
  gamma=N[(etadiel-etaair)/(etadiel+etaair)];

  etrans=N[p*(1-gamma^2)/(1-(gamma^2)(p^2))];
  powerpersqm=(Abs[etrans]^2)/(2*etaair);

  Return[N[powerpersqm]];
];

eenergystored[freq_epsrdiel_d_sigma_]:=
Block[
  {omega,gammadiel,alpha,beta,etadiel,p,gamma,
  e2plus,e2minus,eenergypersqm},

  omega=N[2*Pi*freq];
  gammadiel=N[I*omega*Sqrt[mu0*eps0*epsrdiel]*
    Sqrt[1+sigma/(I*omega*eps0*epsrdiel)]];
  alpha=Re[gammadiel];
  beta=Im[gammadiel];
  etadiel=
    N[Sqrt[mu0/(eps0*epsrdiel+sigma/(I*omega))]];
  p=N[E^(-gammadiel*d)];
  gamma=N[(etadiel-etaair)/(etadiel+etaair)];

  e2plus=N[(gamma+1)/(1-(gamma^2)(p^2))];
  e2minus=N[(-gamma*p^2)*(gamma+1)/
    (1-(gamma^2)(p^2))];

  eenergypersqm=
    I*omega*epsrdiel*eps0/4*
    ((Abs[e2minus]^2)/alpha*(E^(2*alpha*d)-1)-
    (Abs[e2plus]^2)/alpha*(E^(-2*alpha*d)-1)+
    (2/beta)*Re[e2plus*Conjugate[e2minus]*
    I*(E^(-2*I*beta*d)-1)]);

```

```

Return[N[eenergypersqm]];
];

henergystored[freq_,epsrdiel_,d_,sigma_]:=
Block[
{omega,gammadiel,alpha,beta,etadiel,p,gamma,
e2plus,e2minus,henergypersqm},

omega=N[2*Pi*freq];
gammadiel=N[I*omega*Sqrt[mu0*eps0*epsrdiel]*
Sqrt[1+sigma/(I*omega*eps0*epsrdiel)]];
alpha=Re[gammadiel];
beta=Im[gammadiel];
etadiel=
N[Sqrt[mu0/(eps0*epsrdiel+sigma/(I*omega))]];
p=N[E^(-gammadiel*d)];
gamma=N[(etadiel-etaair)/(etadiel+etaair)];

e2plus=N[(gamma+1)/(1-(gamma^2)(p^2))];
e2minus=N[(-gamma*p^2)*(gamma+1)/
(1-(gamma^2)(p^2))];

henergypersqm=
I*omega*mu0/(4*Abs[etadiel]^2)*
((Abs[e2minus]^2)/alpha*(E^(2*alpha*d)-1)-
(Abs[e2plus]^2)/alpha*(E^(-2*alpha*d)-1)-
(2/beta)*Re[e2plus*Conjugate[e2minus]*
I*(E^(-2*I*beta*d)-1)]);

Return[N[henergypersqm]];
];

```

A.2 Absorber Design Equations

The following equations were used to generate the data for the plots in section 3.

```

eps0=8.854*10^-12;
mu0=4*Pi*10^-7;
pinc=1.0/377.0/2.0;

```

```

gammaair=N[I*omega*Sqrt[mu0*eps0]];
etaair=N[Sqrt[mu0/eps0]];

```

```

pabs[freq_,epsrdiel_,d_,sigma_]:=

```

```

Block[
  {omega,gammadiel,alpha,beta,etadiel,p,gamma,
  e2plus,e2minus,powerpersqm},

  omega=N[2*Pi*freq];
  gammadiel=N[I*omega*Sqrt[mu0*eps0*epsrdiel]*
  Sqrt[1+sigma/(I*omega*eps0*epsrdiel)]];
  alpha=Re[gammadiel];
  beta=Im[gammadiel];
  etadiel=
  N[Sqrt[mu0/(eps0*epsrdiel+sigma/(I*omega))]];
  p=N[E^(-gammadiel*d)];
  gamma=N[(etadiel-etaair)/(etadiel+etaair)];

  e2plus=N[(gamma+1)/(1-(gamma^2)(p^2))];
  e2minus=N[(-gamma*p^2)*(gamma+1)/
  (1-(gamma^2)(p^2))];

  powerpersqm=N[sigma/(4*alpha)*
  ((Abs[e2minus]^2)*(E^(2*alpha*d)-1)-
  (Abs[e2plus]^2)*(E^(-2*alpha*d)-1))+
  sigma/(2*beta)*Re[e2plus*Conjugate[e2minus]*
  I*(E^(-2*I*beta*d)-1)]];

  Return[N[Abs[powerpersqm]]];
];

```

```

erefl[freq_epsrdiel_d_sigma_]:=
Block[
  {omega,gammadiel,alpha,beta,etadiel,p,gamma},

  omega=N[2*Pi*freq];
  gammadiel=N[I*omega*Sqrt[mu0*eps0*epsrdiel]*
  Sqrt[1+sigma/(I*omega*eps0*epsrdiel)]];
  alpha=Re[gammadiel];
  beta=Im[gammadiel];
  etadiel=
  N[Sqrt[mu0/(eps0*epsrdiel+sigma/(I*omega))]];
  p=N[E^(-gammadiel*d)];
  gamma=N[(etadiel-etaair)/(etadiel+etaair)];

  Return[N[Abs[gamma*(1-p^2)/(1-(gamma^2)(p^2))]]];
];

```

```

preflpercent[freq_epsrdiel_d_sigma_]:=
(erefl[freq,epsrdiel,d,sigma]^2)*100.0;

```

```
pabspercent[freq_epsrdiel_d_sigma]:=
  pabs[freq,epsrdiel,d,sigma]/pinc*100.0;
```

A.3 Absorber Design Equations for Complex Material Parameters

The following equations are alternate forms to those in section A.2. The forms here allow for a specification of complex permittivity and complex permeability.

```
eps0=8.854*10^-12;
mu0=4*Pi*10^-7;
pinc=1.0/377.0/2.0;
```

```
gammaair=N[I*omega*Sqrt[mu0*eps0]];
etaair=N[Sqrt[mu0/eps0]];
```

```
pabs[freq_epsrdiel_murdiel_d]:=
  Block[
```

```
    {mudiel,epsdiel,omega,gammadiel,alpha,beta,etadiel,
     p,gamma,e2plus,e2minus,powerpersqm},
```

```
    omega=N[2*Pi*freq];
    mudiel=N[murdiel*mu0];
    epsdiel=N[epsrdiel*eps0];
    gammadiel=N[I*omega*Sqrt[mudiel*epsdiel]];
    alpha=Re[gammadiel];
    beta=Im[gammadiel];
    etadiel=N[Sqrt[mudiel/epsdiel]];
    p=N[E^(-gammadiel*d)];
    gamma=N[(etadiel-etaair)/(etadiel+etaair)];
```

```
    e2plus=N[(gamma+1)/(1-(gamma^2)(p^2))];
    e2minus=N[(-gamma*p^2)*(gamma+1)/
              (1-(gamma^2)(p^2))];
```

```
    powerpersqm=N[omega/4*
                  ((Abs[e2minus]^2)*Im[epsdiel]/alpha*
                   (E^(2*alpha*d)-1)-
                   (Abs[e2plus]^2)*Im[epsdiel]/alpha*
                   (E^(-2*alpha*d)-1)+
                   (2*Im[epsdiel]/beta)*
                   Re[e2plus*Conjugate[e2minus]*
                    I*(E^(-2*I*beta*d)-1)]+
                   (Abs[e2minus]^2)*Im[mudiel]/
```

```

(alpha*Abs[etadiel]^2)*
(E^(2*alpha*d)-1)-
(Abs[e2plus]^2)*Im[mudiel]/
(alpha*Abs[etadiel]^2)*
(E^(-2*alpha*d)-1)-
(2*Im[mudiel]/(beta*Abs[etadiel]^2))*
Re[e2plus*Conjugate[e2minus]*
I*(E^(-2*I*beta*d)-1))];

Return[N[Abs[powerpersqm]]];
];

erefl[freq_,epsrdiel_,murdiel_,d_]:=
Block[
{mudiel,epsdiel,omega,gammadiel,etadiel,p,gamma},

omega=N[2*Pi*freq];
mudiel=N[murdiel*mu0];
epsdiel=N[epsrdiel*eps0];
gammadiel=N[I*omega*Sqrt[mudiel*epsdiel]];
etadiel=N[Sqrt[mudiel/epsdiel]];
p=N[E^(-gammadiel*d)];
gamma=N[(etadiel-etaair)/(etadiel+etaair)];

Return[N[Abs[gamma*(1-p^2)/(1-(gamma^2)(p^2))]]];
];

preflpercent[freq_,epsrdiel_,murdiel_,d_]:=
(erefl[freq,epsrdiel,murdiel,d]^2)*100.0;

pabspercent[freq_,epsrdiel_,murdiel_,d_]:=
pabs[freq,epsrdiel,murdiel,d]/pinc*100.0;

```

Appendix B Computer Processing of Material Parameter Data

```
#define AGREEMENT 0.2
```

```
main()
```

```
{
    register int loop,loop2;
    int num_points,agreement,branch;
    char buffer_arr[80],*buffer=(char*)&buffer_arr;
    double d,port1_offset,port2_offset,dum_double,slope,
           exper_group_delay,branch_group_delay,dissipation_ratio,
           phase_sum,freq_sum,freq2_sum,product_sum;
    double *freq,*p_phase;
    complex mu_r,epsilon_r,temp_s11,temp_s21,dum_complex;
    complex *s11,*s21,*p;
    FILE *input_files11,*input_files21,*output_file;

    freq=NULL;
    p_phase=NULL;
    s11=NULL;
    s21=NULL;
    p=NULL;
    input_files11=NULL;
    input_files21=NULL;
    output_file=NULL;

    freq=(double*)calloc((unsigned)405,(unsigned)sizeof(double));
    if(freq==NULL) {
        printf("Error allocating freq array\n");
        goto stop_program;
    }
    p_phase=(double*)calloc((unsigned)405,(unsigned)sizeof(double));
    if(p_phase==NULL) {
        printf("Error allocating p_phase array\n");
        goto stop_program;
    }
    s11=(complex*)calloc((unsigned)405,(unsigned)sizeof(complex));
    if(s11==NULL) {
        printf("Error allocating s11 array\n");
        goto stop_program;
    }
    s21=(complex*)calloc((unsigned)405,(unsigned)sizeof(complex));
    if(s21==NULL) {
        printf("Error allocating s21 array\n");
    }
}
```

```

    goto stop_program;
}
p=(complex*)calloc((unsigned)405,(unsigned)sizeof(complex));
if(p==NULL) {
    printf("Error allocating p array\n");
    goto stop_program;
}

printf("Input file with s11 data: ");
buffer=cgets(buffer);
input_files11=fopen(buffer,"r");
if(input_files11==NULL) {
    printf("File not found\n");
    goto stop_program;
}

printf("Input file with s21 data: ");
buffer=cgets(buffer);
input_files21=fopen(buffer,"r");
if(input_files21==NULL) {
    printf("File not found\n");
    goto stop_program;
}

printf("Output file : ");
buffer=cgets(buffer);
output_file=fopen(buffer,"w");
if(output_file==NULL) {
    printf("File not found\n");
    goto stop_program;
}

printf("Thickness of Material (cm): ");
buffer=cgets(buffer);
sscanf(buffer,"%lE",&d);
d=d/100.0;

printf("Distance from port 1 ref plane to sample (cm): ");
buffer=cgets(buffer);
sscanf(buffer,"%lE",&port1_offset);
port1_offset=port1_offset/100.0;
printf("Distance from port 2 ref plane to sample (cm): ");
buffer=cgets(buffer);
sscanf(buffer,"%lE",&port2_offset);
port2_offset=port2_offset/100.0;

```

```

num_points=0;
while(!feof(input_files1) && !feof(input_files2)) {
    if(fgets(buffer,80,input_files1)!=NULL) {
        num_points++;
        sscanf(buffer,"%le%le%le",&dum_double,
            &(s11[num_points].rl),&(s11[num_points].im));
        if(fgets(buffer,80,input_files2)!=NULL) {
            sscanf(buffer,"%le%le%le",&freq[num_points],
                &(s21[num_points].rl),&(s21[num_points].im));
/*reference plane adjustments*/
            s11[num_points]=cmult(s11[num_points],cexp(cmplx(0.0,
                2.0*PI*freq[num_points]*2*port1_offset/2.998e8)));
            s21[num_points]=cmult(s21[num_points],cexp(cmplx(0.0,
                2.0*PI*freq[num_points]*(port1_offset+port2_offset
                /2.998e8)));
            s_params_to_gamma_p(d,freq[num_points],s11[num_points],
                s21[num_points],&dum_complex,&(p[num_points]));
        }
    }
}

unwrap_phase(num_points,p,p_phase);

fprintf(output_file,"Frequency\tmu'\tmu''\tpeps'\tpeps''\tsgamma\t
    diss_ratio\n");

for(loop=3;loop<=num_points-2;loop++) {

/*calculate the experimetal group delay by a linear approx of the phase
curve over 5 points*/
    phase_sum=0.0;
    freq_sum=0.0;
    freq2_sum=0.0;
    product_sum=0.0;
    for(loop2=-2;loop2<=2;loop2++) {
        phase_sum+=p_phase[loop+loop2];
        freq_sum+=freq[loop+loop2];
        freq2_sum+=freq[loop+loop2]*freq[loop+loop2];
        product_sum+=freq[loop+loop2]*p_phase[loop+loop2];
    }
    slope=(phase_sum*freq_sum-product_sum*5.0)/
        (freq_sum*freq_sum-freq2_sum*5.0);
    exper_group_delay=-slope/(2.0*PI);

/*loop through branch cuts to see which matches the experimental group
delay*/

```

```

branch=0;
temp_s11=s11[loop];
temp_s21=s21[loop];
s_params_to_material_params(d,freq[loop],temp_s11,temp_s21,
    &mu_r,&epsilon_r,branch);
branch_group_delay=group_delay(d,epsilon_r,mu_r);
agreement=
    fabs((exper_group_delay-branch_group_delay)/
        exper_group_delay)<AGREEMENT;

if(agreement) {

fprintf(output_file,"%E\t%7.4f\t%7.4f\t%7.4f\t%7.4f\t%E\t%E\n",
    freq[loop],mu_r.rl,mu_r.im,epsilon_r.rl,-epsilon_r.im,
    -2.0*PI*freq[loop]*8.854e-12*epsilon_r.im,
    epsilon_r.im/mu_r.im*cmag(cdiv(mu_r,epsilon_r)));

} else {

    branch=1;
    do {
        s_params_to_material_params(d,freq[loop],temp_s11,temp_s21,
            &mu_r,&epsilon_r,branch);
        branch_group_delay=group_delay(d,epsilon_r,mu_r);
        agreement=
            fabs((exper_group_delay-branch_group_delay)/
                exper_group_delay)<AGREEMENT;

        if(agreement) {
fprintf(output_file,"%E\t%7.4f\t%7.4f\t%7.4f\t%7.4f\t%E\t%E\n",
    freq[loop],mu_r.rl,mu_r.im,epsilon_r.rl,-epsilon_r.im,
    -epsilon_r.im/epsilon_r.rl,
    -2.0*PI*freq[loop]*8.854e-12*epsilon_r.im,
    epsilon_r.im/mu_r.im*cmag(cdiv(mu_r,epsilon_r)));
            break;
        }

        branch*=-1;
        if(branch>0) branch++;
        if(branch>=10) {
            printf("Unable to process data at frequency=%E\n",
                freq[loop]);
            break;
        }
    } while(!agreement);
}

```

```

    }
}

stop_program:
    if(freq!=NULL) free(freq);
    if(p_phase!=NULL) free(p_phase);
    if(s11!=NULL) free(s11);
    if(s21!=NULL) free(s21);
    if(p!=NULL) free(p);
    if(input_files11!=NULL) fclose(input_files11);
    if(input_files21!=NULL) fclose(input_files21);
    if(output_file!=NULL) fclose(output_file);
}

/*~~~~~*/
void unwrap_phase(num_points,in_arr,out_arr)
register int num_points;
register complex *in_arr;
register double *out_arr;
{
    register int loop;
    register double pi,curr_phase,prev_phase,accumulate,twopi;

    pi=PI;
    twopi=2.0*pi;

    accumulate=0.0;
    prev_phase=cpha(in_arr[1]);
    out_arr[1]=prev_phase;

    for(loop=2;loop<=num_points;loop++) {
        curr_phase=cpha(in_arr[loop]);
        if(curr_phase>=prev_phase+pi) accumulate-=twopi;
        else if(curr_phase<=prev_phase-pi) accumulate+=twopi;
        out_arr[loop]=curr_phase+accumulate;
        prev_phase=curr_phase;
    }
}

/*~~~~~*/
double group_delay(d,epsilon_r,mu_r)
double d;
complex epsilon_r,mu_r;
{

```

```

double temp1,temp2,temp3,temp4,temp5,temp6,temp7,temp8;

temp1=mu_r.rl*epsilon_r.rl;
temp2=mu_r.rl*epsilon_r.im;
temp3=mu_r.im*epsilon_r.rl;
temp4=mu_r.im*epsilon_r.im;

temp5=temp1-temp4;
temp5*=temp5;
temp6=temp2+temp3;
temp6*=temp6;
temp7=temp5-temp6;
if(temp7<=0.0) return 0.0;
temp7=sqrt(temp7);
temp8=temp1-temp4+temp7;
if(temp8<=0.0) return 0.0;
temp8=sqrt(temp8);
return (temp8*d/(2.998e8*sqrt(2.0)));
}

/*~~~~~*/
void material_params_to_s_params(d,freq,s11,s21,mu_r,epsilon_r)
double d,freq;
complex *s11,*s21,mu_r,epsilon_r;
{
    double omega;
    complex gamma,p,c1,z2,prop_const2,ctemp1,ctemp2,
        ctemp3,ctemp4,ctemp5,ctemp6;

/*constants*/
    c1=cmplx(1.0,0.0);

/*calculated values*/
    omega=2.0*PI*freq;

/*calculate intrinsic impedance of region 2*/
    ctemp1=cdiv(mu_r,epsilon_r);
    z2=csqrt(ctemp1);

/*calculate propagation constant of region 2*/
    ctemp1=cmult(mu_r,epsilon_r);
    ctemp2=csqrt(ctemp1);
    prop_const2=cmult(cmplx(0.0,omega/2.998e8),ctemp2);

/*calculate p*/

```

```

    ctemp1=cmult(cmplx(-d,0.0),prop_const2);
    p=cexp(ctemp1);

/*calculate gamma*/
    ctemp1=csub(z2,c1);
    ctemp2=cadd(z2,c1);
    gamma=cdiv(ctemp1,ctemp2);

/*calculate s11*/
    ctemp1=cmult(p,p);
    ctemp2=cmult(gamma,gamma);
    ctemp3=csub(c1,ctemp1);
    ctemp4=cmult(ctemp3,gamma);
    ctemp5=cmult(ctemp1,ctemp2);
    ctemp6=csub(c1,ctemp5);
    *s11=cdiv(ctemp4,ctemp6);

/*calculate s21*/
    ctemp1=cmult(gamma,gamma);
    ctemp2=cmult(p,p);
    ctemp3=csub(c1,ctemp1);
    ctemp4=cmult(ctemp3,p);
    ctemp5=cmult(ctemp1,ctemp2);
    ctemp6=csub(c1,ctemp5);
    *s21=cdiv(ctemp4,ctemp6);
}

/*~~~~~*/
void s_params_to_material_params(d,freq,s11,s21,mu_r,epsilon_r,branch)
double d,freq;
complex s11,s21,*mu_r,*epsilon_r;
int branch;
{
    complex gamma,p,chi,x,y,c1,ctemp1,ctemp2,
        ctemp3,ctemp4,ctemp5,ctemp6,ctemp7;

/*constants*/
    c1=cmplx(1.0,0.0);

/*calculate gamma*/
    ctemp1=csub(cmult(s11,s11),cmult(s21,s21));
    ctemp2=cadd(ctemp1,c1);
    ctemp3=cmult(cmplx(2.0,0.0),s11);
    chi=cdiv(ctemp2,ctemp3);

```

```

    ctemp4=csub(cmult(chi,chi),c1);
    ctemp5=csqrt(ctemp4);
    ctemp6=cadd(chi,ctemp5);
    ctemp7=csub(chi,ctemp5);
    if(cmag(ctemp6)<=1) gamma=ctemp6;
    else gamma=ctemp7;

/*calculate p*/
    ctemp1=cadd(s11,s21);
    ctemp2=csub(ctemp1,gamma);
    ctemp3=cmult(ctemp1,gamma);
    ctemp4=csub(c1,ctemp3);
    p=cdiv(ctemp2,ctemp4);

/*calculate x*/
    ctemp1=cadd(c1,gamma);
    ctemp2=csub(c1,gamma);
    x=cdiv(ctemp1,ctemp2);

/*calculate y*/
    ctemp1=cmplx(0.0,-2.998e8/(2.0*PI*freq*d));
    ctemp2=cdiv(c1,p);
    ctemp3=cln(ctemp2,branch);
    y=cmult(ctemp1,ctemp3);
    if(y.rl<0.0) y=cmult(y,cmplx(-1.0,0.0));

/*calculate mu and epsilon*/
    *mu_r=cmult(x,y);
    *epsilon_r=cdiv(y,x);
}

/*~~~~~*/
void s_params_to_gamma_p(d,freq,s11,s21,gamma,p)
double d,freq;
complex s11,s21,*gamma,*p;
{
    double omega;
    complex chi,x,y,c1,ctemp1,ctemp2,ctemp3,ctemp4,ctemp5,ctemp6,ctemp7;

/*constants*/
    c1=cmplx(1.0,0.0);

/*calculated values*/
    omega=2.0*PI*freq;

```

```

/*calculate gamma*/
  ctemp1=csub(cmult(s11,s11),cmult(s21,s21));
  ctemp2=cadd(ctemp1,c1);
  ctemp3=cmult(cmplx(2.0,0.0),s11);
  chi=cdiv(ctemp2,ctemp3);
  ctemp4=csub(cmult(chi,chi),c1);
  ctemp5=csqrt(ctemp4);
  ctemp6=cadd(chi,ctemp5);
  ctemp7=csub(chi,ctemp5);
  if(cmag(ctemp6)<=1) *gamma=ctemp6;
  else *gamma=ctemp7;

/*calculate p*/
  ctemp1=cadd(s11,s21);
  ctemp2=csub(ctemp1,*gamma);
  ctemp3=cmult(ctemp1,*gamma);
  ctemp4=csub(c1,ctemp3);
  *p=cdiv(ctemp2,ctemp4);
}

/*~~~~~*/
void gamma_p_to_s_params(d,freq,gamma,p,s11,s21)
double d,freq;
complex gamma,p,*s11,*s21;
{
  double omega;
  complex c1,ctemp1,ctemp2,ctemp3,ctemp4,ctemp5,ctemp6;

/*constants*/
  c1=cmplx(1.0,0.0);

/*calculated values*/
  omega=2.0*PI*freq;

/*calculate s11*/
  ctemp1=cmult(p,p);
  ctemp2=cmult(gamma,gamma);
  ctemp3=csub(c1,ctemp1);
  ctemp4=cmult(ctemp3,gamma);
  ctemp5=cmult(ctemp1,ctemp2);
  ctemp6=csub(c1,ctemp5);
  *s11=cdiv(ctemp4,ctemp6);
}

```

```

/*calculate s21*/
    ctemp1=cmult(gamma,gamma);
    ctemp2=cmult(p,p);
    ctemp3=csub(c1,ctemp1);
    ctemp4=cmult(ctemp3,p);
    ctemp5=cmult(ctemp1,ctemp2);
    ctemp6=csub(c1,ctemp5);
    *s21=cdiv(ctemp4,ctemp6);

}

/*~~~~~*/
void
gamma_p_to_material_params(d,freq,gamma,p,mu_r,epsilon_r,branch)
double d,freq;
complex gamma,p,*mu_r,*epsilon_r;
int branch;
{
    double omega;
    complex x,y,c1,ctemp1,ctemp2,ctemp3,ctemp4,ctemp5,ctemp6,ctemp7;

/*constants*/
    c1=cmplx(1.0,0.0);

/*calculated values*/
    omega=2.0*PI*freq;

/*calculate x*/
    ctemp1=cadd(c1,gamma);
    ctemp2=csub(c1,gamma);
    ctemp3=cdiv(ctemp1,ctemp2);
    x=cmult(ctemp3,ctemp3);

/*calculate y*/
    ctemp1=cmplx(3.0e8/(omega*d),0.0);
    ctemp2=cdiv(c1,p);
    ctemp3=cln(ctemp2,branch);
    ctemp4=cmult(ctemp1,ctemp3);
    ctemp5=cmult(ctemp4,ctemp4);
    y=cmult(cmplx(-1.0,0.0),ctemp5);

/*calculate mu*/
    ctemp1=cmult(x,y);
    *mu_r=csqrt(ctemp1);

```

```

/*calculate epsilon*/
  ctemp1=cdiv(y,x);
  *epsilon_r=csqrt(ctemp1);
)

typedef struct {
  double rl,im;
} complex;

complex cmplx(r1,r2)
double r1,r2;
{
  complex temp;

  temp.rl=r1;
  temp.im=r2;
  return temp;
}

double cmag(z1)
complex z1;
{
  return sqrt(z1.rl*z1.rl+z1.im*z1.im);
}

double cmag2(z1)
complex z1;
{
  return (z1.rl*z1.rl+z1.im*z1.im);
}

double cpha(z1)
complex z1;
{
  double pha;

  if(z1.rl==0.0) {
    if(z1.im==0.0) return 0.0;
    if(z1.im>0.0) return PI/2.0;
    return -PI/2.0;
  }
  pha=atan(z1.im/z1.rl);
  if(z1.rl<0.0) return (pha+PI);
}

```

```

    return pha;
}

complex cadd(z1,z2)
complex z1,z2;
{
    complex temp;

    temp.rl=z1.rl+z2.rl;
    temp.im=z1.im+z2.im;
    return temp;
}

complex csub(z1,z2)
complex z1,z2;
{
    complex temp;

    temp.rl=z1.rl-z2.rl;
    temp.im=z1.im-z2.im;
    return temp;
}

complex cmult(z1,z2)
complex z1,z2;
{
    complex temp;

    temp.rl=z1.rl*z2.rl-z1.im*z2.im;
    temp.im=z1.rl*z2.im+z1.im*z2.rl;
    return temp;
}

complex cdiv(z1,z2)
complex z1,z2;
{
    complex temp;
    double rtemp;

    rtemp=cmag2(z2);
    temp.rl=(z1.rl*z2.rl+z1.im*z2.im)/rtemp;
    temp.im=(z1.im*z2.rl-z1.rl*z2.im)/rtemp;
    return temp;
}

complex cexp(z1)

```

```

complex z1;
{
    complex temp;
    double decay;

    decay=exp(z1.rl);
    temp.rl=decay*cos(z1.im);
    temp.im=decay*sin(z1.im);
    return temp;
}

```

```

complex conj(z1)
complex z1;
{
    complex temp;

    temp.rl=z1.rl;
    temp.im=-z1.im;
    return temp;
}

```

```

complex cp2r(z1)
complex z1;
{
    /*when sent a polar complex with magnitude in real part and
    phase (radians) in imaginary part, this returns a rectangular complex*/

    complex temp;

    temp.rl=z1.rl*cos(z1.im);
    temp.im=z1.rl*sin(z1.im);
    return temp;
}

```

```

complex cr2p(z1)
complex z1;
{
    /*when sent a rectangular complex, this returns a polar complex with
    magnitude in real part and phase (radians) in imaginary part*/

    complex temp;

    temp.rl=cmag(z1);
    temp.im=cpha(z1);
    return temp;
}

```

```

complex csqrt(z1)
complex z1;
{
    complex temp;

    temp=cr2p(z1);
    temp.rl=sqrt(temp.rl);
    temp.im=temp.im/2.0;
    temp=cp2r(temp);
    return temp;
}

```

```

complex croot(z1,n,i)
complex z1;
int n,i;
{
    /*returns the ith value of z1**(1/n)
    i is between 0 and n-1
    */
    complex ctemp;
    register double mag,phase,dn;

    dn=(double)n;
    ctemp=cr2p(z1);
    mag=pow(ctemp.rl,1.0/dn);
    phase=(ctemp.im+2.0*PI*i)/dn;
    ctemp=cmplx(mag*cos(phase),mag*sin(phase));
    return ctemp;
}

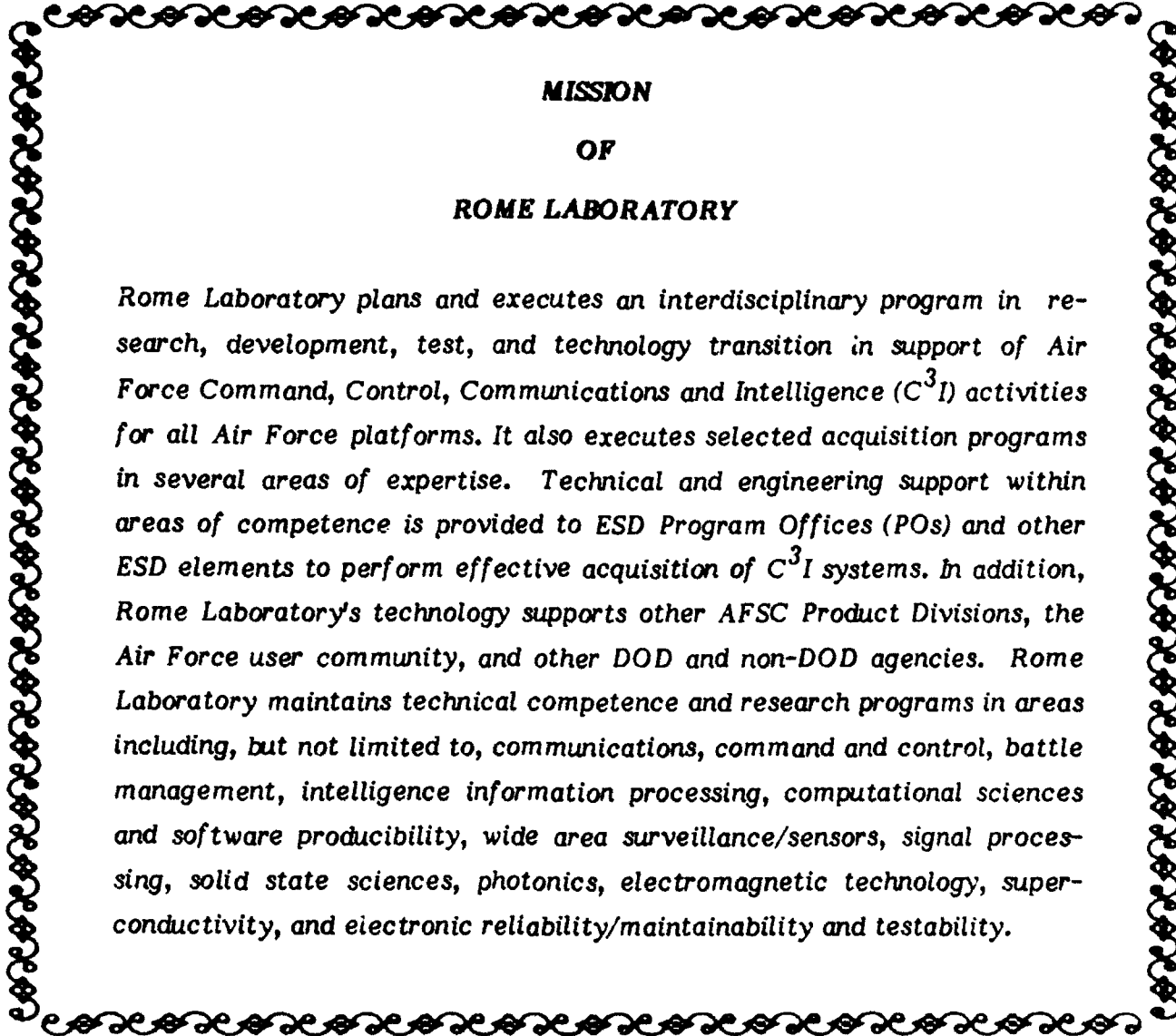
```

```

complex cln(z1,branch)
complex z1;
int branch;
{
    complex temp;

    temp.rl=log(cmag(z1));
    temp.im=cpha(z1)+2.0*PI*branch;
    return temp;
}

```



**MISSION
OF
ROME LABORATORY**

Rome Laboratory plans and executes an interdisciplinary program in research, development, test, and technology transition in support of Air Force Command, Control, Communications and Intelligence (C³I) activities for all Air Force platforms. It also executes selected acquisition programs in several areas of expertise. Technical and engineering support within areas of competence is provided to ESD Program Offices (POs) and other ESD elements to perform effective acquisition of C³I systems. In addition, Rome Laboratory's technology supports other AFSC Product Divisions, the Air Force user community, and other DOD and non-DOD agencies. Rome Laboratory maintains technical competence and research programs in areas including, but not limited to, communications, command and control, battle management, intelligence information processing, computational sciences and software producibility, wide area surveillance/sensors, signal processing, solid state sciences, photonics, electromagnetic technology, superconductivity, and electronic reliability/maintainability and testability.